Continuous and Non-invasive Blood Pressure Monitoring using Ultrasonic Methods

by

Joohyun Seo

B.S. in Electrical Engineering
Seoul National University (2012)

Submitted to the Department of Electrical Engineering and Computer Science
in partial fulfillment of the requirements for the degree of

Master of Science in Electrical Engineering and Computer Science

at the

MASSACHUSETTS INSTITUTE OF TECHNOLOGY

June 2014

Signature redacted

Author .....
Department of Electrical Engineering and Computer Science
May 21, 2014

Signature redacted

Certified by ....
Hae-Seung Lee
ATSP Professor of Electrical Engineering
Thesis Supervisor

Signature redacted

Certified by .. ..
Charles G. Sodini
Lebel Professor of Electrical Engineering
Thesis Supervisor

Signature redacted

Accepted by ....
Leslie A. Kolodziejski
Chair, Department Committee on Graduate Students

Continuous and Non-invasive Blood Pressure Monitoring using Ultrasonic Methods

by

Joohyun Seo

Submitted to the Department of Electrical Engineering and Computer Science
on May 21, 2014, in partial fulfillment of the
requirements for the degree of
Master of Science in Electrical Engineering and Computer Science

Abstract

This thesis presents a continuous and non-invasive arterial blood pressure (CNAP) monitoring technique using ultrasound. An arterial blood pressure (ABP) waveform provides valuable information in treating cardiovascular diseases. Although an invasive ABP measurement through arterial catheterization performed in an intensive care unit (ICU) is considered a gold standard, its invasive nature not only increases various patients' risks but makes its usage for cardiovascular studies expensive. Therefore, reliable non-invasive ABP waveform estimation has been desired for a long time by medical communities.

This work details ABP waveform estimation based on a vessel cross-sectional area measurement combined with the elastic property of an arterial vessel, represented by a pulse wave velocity (PWV). Several ultrasound techniques including uniform insonation and echo-tracking are explored to measure the PWV using so-called QA method as well as the cross-sectional area. The physiological background of the arterial system and considerations for a clinical test are also presented.

Experimental results validate the QA method and the proposed ABP waveform estimation method in a custom-designed experimental setup consisting of a diaphragm pump and a latex rubber tube using two commercially available single element ultrasonic transducers. The design of a portable CNAP monitoring device using ultrasound will fuel the exponential growth of a readily available, inexpensive but powerful cardiovascular diagnostic tool.

Thesis Supervisor: Hae-Seung Lee
Title: ATSP Professor of Electrical Engineering

Thesis Supervisor: Charles G. Sodini
Title: Lebel Professor of Electrical Engineering

Acknowledgments

First of all, I would like to appreciate my parents for their endless support on my academic journey at the MIT. Certainly, starting a new research project in a foreign country was not smooth, but their emotional support and faith on me as a student and their son have motivated me greatly to complete this Master's thesis. As always, they have been great mentors in my life, and they will be in the future as well.

I would like to express my greatest appreciation to research advisors, Professors Hae-Seung Lee and Charles Sodini. Their exceptional insight and extensive technical knowledge always guide me in the right direction. Besides, their mentorship and advices help me realize and become a better student and researcher. Without their technical guidances, this thesis work could not be completed.

Next, technical advices from Dr. Kai Thomenius (MIT) regarding medical ultrasound have been particularly helpful. His extraordinary knowledge in medical ultrasound helps me increase the depth of this thesis. Also, I would like to thank Dr. Brian Brandt (Maxim Integrated) for his generous interest on this work and for the opportunity of me giving a talk at the Maxim Integrated Boston design center. I also appreciate insightful comments from Dr. Tom O'Dwyer (Analog Devices) from weekly meetings.

Lastly, I thank all my colleagues in 38-265 for me to enjoy delightful office life. Especially, Sabino Pietrangelo and Dr. Kailiang Chen has helped me troubleshoot hardware issues and resolve any difficulties encountered on my research. The constructive discussion with other colleagues on various topics also expands my scope of knowledge not only in medical ultrasound and medical electronics, but also in analog circuit designs and beyond.

This work is partially funded by the MIT Center for Integrated Circuits and Systems (CICS). In addition, Samsung fellowship is appreciated for financial support on my graduate student life at the MIT.

Contents

List of Figures

List of Tables

Chapter 1

Introduction

1.1 Cardiovascular Disease Diagnostics

The world health organization (WHO) defines cardiovascular diseases (CVD) as a group of disorders of the heart and blood vessels. CVDs include coronary heart disease, cerebrovascular disease, peripheral arterial disease, rheumatic heart disease, congenital heart disease, deep vein thrombosis and pulmonary embolism. CVDs related to the heart muscle and the brain are critical because these organs are vital to maintain life. According to the report from the WHO, CVDs are the leading cause of death. The WHO report estimates that 17.3 million people died from CVDs in 2008, which accounts for 30% of global deaths [1]. Of the 17.3 million deaths, the report estimates that 7.3 million were due to the coronary heart disease (i.e., the CVD of the artery supplying blood to the heart muscle), and 6.2 million cases were due to stroke (i.e., the loss of brain function due to reduced blood supply). According to the WHO fact sheets, hypertension accounts for 9.4 million deaths annually, and this figure includes 51% of deaths caused by the stroke and 45% by the coronary heart disease. Since the stroke and heart attack are acute and generally life-threatening, a significant amount of research has been conducted to identify a risk factor for these diseases.

In general, the study of the human circulatory system is of great importance because it delivers oxygen and nutrition as well as removes carbon dioxide and waste

to sustain metabolism and respiration. For CVD studies and diagnosis, various tools have been developed, validated and clinically accepted. For example, an electrocardiogram (ECG; recordings of body surface potential) assesses the electrical functionality of the heart, which is depolarization followed by repolarization as the atria and ventricles successively contract. Because of its non-invasive and practical nature, the ECG signal has been broadly used in both ambulatory, and at the bedside. The normal ECG signal features P wave followed by the QRS complex and T wave successively, and the interpretation of the signal is well established for cardiologists to diagnose various heart diseases (e.g., ventricular tachycardia, ventricular fibrillation) and to make clinical decisions in a timely manner.

Also, the anatomy of the vascular system has been studied in a non-invasive manner with the help of various imaging modalities such as ultrasonography, computed tomography (CT), angiography and magnetic resonance imaging (MRI). Doppler spectrogram is another good example of a clinically accepted diagnostic technique to examine the circulatory function. The Doppler spectrogram measures blood flow velocity based on the Doppler effect of an acoustic wave. With the spectrogram, physicians and sonographers diagnose vascular diseases such as arteriosclerosis or measure cardiac output (i.e., blood volume pumped by the heart for one minute).

Finally, blood pressure, more often referred to as arterial blood pressure (ABP), is a key physiological parameter in assessing the circulatory system. Oftentimes, the blood pressure is measured by a sphygmomanometer with an inflatable cuff wrapped around the upper extremity. At the beginning of measurement, the cuff occludes the brachial artery completely and release pressure until the artery just starts open at the systolic stage to measure systolic blood pressure. Then, it continues to release pressure until the artery remains open for an entire cardiac cycle to measure diastolic blood pressure. Because of the simplistic usage and non-invasive nature, the sphygmomanometer became a primary instrument to measure blood pressure. However, it produces only systolic and diastolic blood pressure measurements at one moment, which are highly undersampled measurements in time and insufficient to truly represent the dynamic behavior of the cardiovascular system.

A complete ABP waveform is only available in an intensive care unit (ICU) of hospitals. On heavily monitored ICU patients, the radial or the femoral artery is accessed through arterial catheterization. This procedure provides a pathway to adminster drugs directly to the arterial system, instead of intravaneous methods, to collect an arterial blood sample for laboratory tests such as arterial blood gas and to measure the ABP waveform. A pressure sensor connected via a rigid tubing to an arterial catheter directly reads the ABP waveform although a pressure wire is occasionally inserted to obtain the ABP waveform at different arterial sites. The ABP waveform truly reflects hemodynamic phenomena, and the waveform itself is a rich source of information for CVD research.

1.2 Motivation

The ABP waveform provides valuable information of the circulatory system of patients. By analyzing the ABP waveform, a powerful predictor for CVDs is often found. For example, high pulse pressure (PP; difference between systolic and diastolic blood pressure) was reported as a risk factor for the coronary heart disease in the middle-aged and elderly [2]. Similarly, the pulsatility of ascending aortic pressure was found as a strong predictor for recurrence of stenosis (i.e., narrowing of blood vessel) after percutaneous transluminal coronary angioplasty [3].

In addition, various physiological parameters derived from the ABP waveform not only assist hospital staff to make clinical decisions but allow them to navigate complicated relations between hemodynamics parameters. For instance, a continuous cardiac output (CO) monitoring method using a peripheral ABP waveform was proposed and verified with a swine experiment [4]. Following this study, monitoring continuous CO and total peripheral resistance (TPR) over various ambulatory activities was introduced [5]. In addition to these studies, an adaptive transfer function to derive a central ABP waveform from the peripheral ABP waveform was proposed to find a better indicator for hemmorhage, which potentially benefits battlefield medicine [6]. These examples testify indispensability of the ABP waveform in cardiovascular re-

search.

Unfortunately, the ABP waveform is typically obtained only through the arterial catheterization as mentioned previously. Although considered a gold standard, the disadvantage of this method is its invasive nature. This invasive nature unavoidably increases the possibility of infection through the artery as well as damage to adjacent tissue because the artery usually lies deep below the skin. The anticipated patients' risks tend to confine the usage of the ABP waveform obtained by arterial catheterization in critical-care decisions. In addition, the ABP waveform is used limitedly in cardiovascular research because the waveform is not readily obtainable.

Currently, some non-invasive ABP waveform monitoring techniques have been introduced to overcome the limitation of the gold standard method, and they fall mainly into two categories: arterial tonometry and a volume clamp. The arterial tonometry is a transcutaneous pulse sensing technique to directly determine the blood pressure inside an artery. A tonometer applies enough pressure to distort the vessel until normal contact stress between the skin and the tonometer surface becomes the same as blood pressure [7]. In general, tonometry requires a superficial artery with a desirable size supported by a hard structure such as bones. Because of this requirement, tonometry cannot be applied to all patients and arterial sites [8]. For example, the quality of the pressure measurement from obese patients is poor. In addition, the measurement at femoral artery using applanation tonometry was found unreliable in a large number of subjects [8].

The volume clamp type is based on the method reported by Penaz [9]. This type of device applies external pressure with an inflatable finger cuff while measuring blood volume through an infrared photoplethysmograph. Blood volume measured by the plethysmograph is clamped by adjusting the cuff pressure to match the blood pressure change, and the cuff pressure is read as the blood pressure measurement [10]. A volume clamp point is set to make the artery only partially occluded to keep reasonable oxygenation level of the finger tip. The accuracy of this device has been investigated in articles to compare it to intra arterial blood pressure recording [10,11]. Also, this type of device was also utilized to obtain the peripheral ABP waveform [5,6].

Although the performance of the device continues to improve, it only measures the finger ABP waveform and requires the cuff, thus lessening patients' comfort for long term monitoring with reduced blood flow to the finger tip.

In order to overcome some of these limitations, ultrasonography appears as a viable option because it is a promising non-invasive imaging modality in investigating both vascular anatomy and hemodynamics of patients. Compared to other modalities, such as CT and MRI, medical ultrasound is far less expensive, free of radiation and potentially suitable to portable system implementation. Because of these benefits, medical ultrasound has already been widely adopted for daily screening, subcutaneous tissue structure imaging and medical diagnostics such as obstetric sonography. Therefore, the ABP waveform monitoring using ultrasound is a particularly intriguing research issue not only because of its non-invasive nature but because of its cost efficiency and potential aptness for a portable medical device. Additionally, an ultrasound approach eliminates the necessity for the inflatable cuff, thereby promoting patients' comfort desirable for long-term monitoring.

1.3 Objective of Thesis Work

The main objective of this thesis work is to address the ABP waveform estimation technique using physiological waveforms obtained by various ultrasound techniques and to experimentally verify the effectiveness of the technique. The following six aims detail the main objective:

- Background
  - To provide background in medical ultrasonography
  - To describe the behavior of the ABP waveform in the human arterial system on the basis of hemodynamics
- Experimental Validation
  - To estimate flow velocity using pulsed Doppler ultrasound.
  - To estimate a full diameter waveform using an echo-tracking method.

- To estimate a local pulse wave velocity using physiological waveforms
- To estimate a pressure waveform and compare it with a reference waveform.

Additionally, this thesis work lays the ground work for a future clinical test of the ABP waveform estimation.

1.4 Thesis Organization

This thesis begins with general ultrasound background in Chapter 2. This chapter describes the propagation of an acoustic wave, scattering mechanisms which essentially allow diagnostic ultrasound to work. Chapter 2 continues with acoustic wave generation in a piezoelectric element and its equivalent circuit model followed by the description of acoustic pressure field patterns in both continuous and pulsed waves.

The anatomical background of the human arterial system relevant to the ABP measurement is described in Chapter 3. This chapter proceeds to blood flow physics and the relationship between physiological parameters such as blood pressure and blood flow. Finally, the behavior of a pulse pressure wave and its propagation speed are analyzed within a simplified elastic tube model.

In Chapter 4, a method to estimate ABP waveform is first described with necessary physiological waveforms: a spatial mean blood velocity and an artery diameter waveform. Several ultrasound methods are introduced and compared with each other. Their benefits and limitations in estimating the physiological waveforms are discussed.

The experimental results of the pressure waveform estimating technique is presented in Chapter 5. This chapter characterizes a custom designed experimental setup and explains experimental procedures. The experimental results begin with pressure sensor calibration, spatial mean velocity estimation, local pulse wave velocity estimation followed by the verification of the pressure waveform estimation. Chapter 6 discusses the key contribution of this thesis work and addresses future works.

This thesis includes many results of acoustic field simulation conducted in Field II ultrasound simulation program [12, 13].

Chapter 2

General Ultrasound Background

This chapter describes a basic theory of operation of ultrasonography. The ultrasonography is an imaging or diagnostic technique using ultrasound which is defined as a longitudinal acoustic wave above audible frequencies. This chapter gives a theoretical view mainly in two aspects: an acoustic wave theory and ultrasound transducer design and characterization. The following section defines variables in the acoustic wave theory and describes the interaction of the acoustic wave with tissue via absorption and scattering.

2.1 Acoustic Wave in Tissue

2.1.1 Acoustic Wave Propagation

An acoustic wave can propagate through all phases of matter: gas, liquid and solid, and the propagation mode may differ from phase to phase. In diagnostic ultrasound, the analysis of acoustic wave propagation in water sets basis because the acoustic characteristics of tissue, which mainly consists of water, is fairly similar to that of water. Although the exact characterization of tissue as a medium also involves nonlinearity and complicatedness, a linear analysis in water provides an insight of the overall wave behavior. Additionally, only the longitudinal wave exists in water, which keeps the analysis simple [14].

The following analytics is based on the assumption that the medium is an idealized inviscid fluid [14]. As the acoustic wave propagates, particles in the medium are displaced from its resting position in an oscillatory manner. The displacement results in local pressure disturbance as a result of the compression and expansion of the medium. A particle velocity (v) is expressed as, by definition,

$$v(\vec{r},t) = \frac{\partial u(\vec{r},t)}{\partial t} \tag{2.1}$$

where u is a displacement. For convenience of analysis, a velocity potential (ϕ) is defined as

$$v(\vec{r},t) = \nabla\phi(\vec{r},t) \tag{2.2}$$

Then, a pressure (p) is defined in terms of the velocity potential as

$$p(\vec{r},t) = -\rho\frac{\partial\phi(\vec{r},t)}{\partial t} \tag{2.3}$$

where ρ is the density of fluid at rest. An acoustic wave equation is written in three dimensional space as

$$\nabla^2\phi(\vec{r},t) - \frac{1}{c^2}\frac{\partial^2\phi(\vec{r},t)}{\partial t^2} = 0 \tag{2.4}$$

where c is the speed of sound. The speed of sound is determined by properties of the medium which are the isothermal bulk modulus (B_T), the ratio of specific heats (γ) and the density (ρ).

$$c = \sqrt{\frac{\gamma B_T}{\rho}} \tag{2.5}$$

The solution of the wave equation indicates two waves traveling in forward and backward direction. A specific acoustic impedance is defined as the ratio of pressure to the particle velocity in a forward traveling wave. The acoustic impedance has a unit of $\mathrm{kg/m^2 \cdot s}$, also known as *Rayls*. Typical acoustic parameters of water, tissue and blood are summarized in Table 2.1.

An instantaneous intensity (I_{inst}) is expressed in terms of the acoustic impedance as:

$$Z = \frac{p}{v} = \rho c \tag{2.6}$$

Table 2.1: Acoustic parameters in biological media from [15, 16]

Medium	**Density (kg/m^3)**	**Acoustic Impedance (MRayls)**	**Speed of Sound (m/s)**
Air	1.2	0.0004	333
Water	998	1.48	1481
Blood	1060	1.66	1566
Soft Tissue (average)	1058	1.63	1540

$$I_{inst} = \frac{p(\vec{r},t)p^*(\vec{r},t)}{Z} = v(\vec{r},t)v^*(\vec{r},t)Z \tag{2.7}$$

Instead of the instantaneous intensity, an averaged intensity in either a temporal or a spatial domain delivers the clear view of acoustic energy transfer. Also, the intensity is certainly an essential parameter in safety consideration [17]. A spatial-average (SA) intensity provides the sense of total power generated by an ultrasonic transducer while a spatial-peak (SP) intensity or maximum intensity is more pertinent to the safety. Meanwhile, a temporal-average (TA) intensity results in the spatial pattern of an acoustic field, and this pattern, also known as a beam pattern, is important in diagnostic ultrasound because the beam pattern is not usually uniform in the region of interest. The usage and performance of an ultrasound system relies on defining the desirable beam pattern, which is typically evaluated in terms of the TA intensity. In case the acoustic wave is pulsed, a pulse-average (PA; average over pulse cycles) intensity is also used as a substitute for the TA intensity [17].

2.1.2 Acoustic Wave Scattering

An acoustic wave gradually loses its energy as it propagates through biological tissues. This energy loss is mainly attributed to two phenomena: absorption and scattering [18]. A plane wave attenuated as it travels is expressed as:

$$u(\vec{r},t) = u_0 e^{-\alpha z} e^{i\omega(t-\frac{z}{c})} \tag{2.8}$$

where α is known as an attenuation coefficient. The exact attenuation coefficient changes among various tissues and also increases as the frequency of the acoustic wave rises. The dependency of the attenuation coefficient on frequency comes from stronger diffusive scattering at a higher frequency, which is discussed in the following paragraphs. Typically, the attenuation coefficient in soft tissue is 1 dB/cm at 2 MHz [17].

Absorption in tissue usually refers to energy transfer from acoustic energy to other forms of energy such as heat. Therefore, the safety regulation of diagnostic and therapeutic ultrasound ensures to prevent tissue damage caused by excessive heating. The acoustic scattering not only weakens the propagating wave but, most importantly, makes the acoustic wave return and excite the ultrasonic transducer so that hospital staff can interpret a detected signal to diagnose patients.

The scattering occurs when the acoustic wave propagates through inhomogeneous medium and results in radiating secondary waves. Three types of the scattering mechanism exist, and the mechanism at the medium boundary is categorized depending on the dimension or roughness of the boundary relative to the wavelength of the incident acoustic wave: specular scattering (i.e., reflection), diffusive scattering and diffractive scattering [14].

Specular Scattering

The specular scattering occurs when the roughness of an object or the boundary is much greater than the wavelength of the acoustic wave, and it can be simply understood as reflection. A ray theory is sufficient to explain the trajectories of both a reflected and a transmitted wave as shown in Figure 2-1. In biological tissue, the boundary of organs, bones and other macro structures falls into this type. By solving boundary conditions, which states that the pressure and the particle velocity are continuous, and tangential components of wavenumbers match, the angle of transmission (θ_T) is predicted by snell's law as [14]

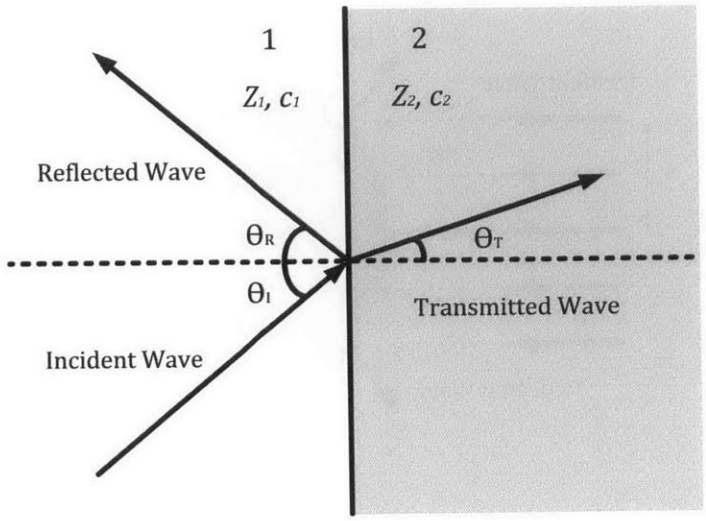

Figure 2-1: Oblique incident wave on a boundary between media with different acoustic impedances

$$\frac{\sin\theta_I}{\sin\theta_T} = \frac{c_1}{c_2} \tag{2.9}$$

where c_1 and c_2 are the speed of sound in medium 1 and 2, respectively. At the same time, the angle of reflection (θ_R) is equal to the angle of incidence (θ_I) dictated by the ray theory. Since the wavenumber component normal to the boundary has cosine dependency, effective acoustic impedances of medium 1 and 2 are expressed as

$$Z_{1\theta_I} = \frac{\rho_1 c_1}{\cos\theta_I} = \frac{Z_1}{\cos\theta_I} \tag{2.10a}$$

$$Z_{2\theta_T} = \frac{\rho_2 c_2}{\cos\theta_T} = \frac{Z_2}{\cos\theta_T} \tag{2.10b}$$

where ρ_1 and ρ_2 are the density of medium 1 and 2, respectively. As a result, a reflection factor (RF) and a transmission factor (TF) are given by:

$$RF = \frac{Z_{2\theta_T} - Z_{1\theta_I}}{Z_{2\theta_T} + Z_{1\theta_I}} = \frac{Z_2\cos\theta_I - Z_1\cos\theta_T}{Z_2\cos\theta_I + Z_1\cos\theta_T} \tag{2.11a}$$

$$TF = \frac{2Z_{2\theta_T}}{Z_{2\theta_T} + Z_{1\theta_I}} = \frac{2Z_2\cos\theta_I}{Z_2\cos\theta_I + Z_1\cos\theta_T} \tag{2.11b}$$

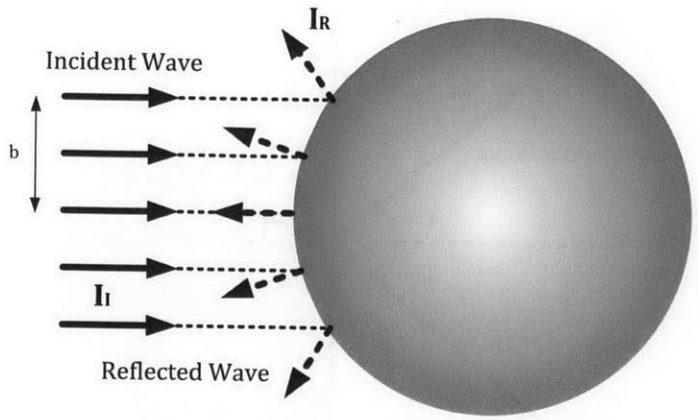

Figure 2-2: Specular scattering of a planar incident wave on a spherical object

Figure 2-2 illustrates the specular scattering at a spherical object with a plane incident wave. Assuming the cross-section of the incident beam is a circle with the radius of b, the intensity ratio of a reflected wave (I_R) to a incident wave (I_I) is given as [14]:

$$\frac{I_R(r)}{I_I} \sim \frac{\pi b^2}{4\pi r^2}|RF|^2 \tag{2.12}$$

where r is approximately the distance from the object. The intensity of the reflected wave is inversely proportional to r^2 and directly proportional to $|RF|^2$.

Diffusive Scattering

In biological tissue, micro structures and scattering objects whose sizes are in sub-wavelength scale also cause scattering in a different mechanism, called diffusive scattering. Provided that the wavelength of diagnostic ultrasound ranges from 150 to 770 μm for an operating frequency from 2 to 10 MHz, most of scattering falls into the diffusive scattering. Contrary to the specular scattering, the diffusive scattering occurs when the roughness of the boundary is much smaller than the wavelength of an incident wave. While the specular scattering helps visualize distinct boundaries between different tissues, the diffusive scattering allows to display different patterns produced from different tissue structures. Therefore, tissue is often modeled as a set of small scatterers, defined as objects to cause scattering, of a sub-wavelength

scale. In addition, the diffusive scattering caused by erythrocytes (i.e., red blood cells) essentially enables Doppler ultrasound to estimate a blood flow velocity. The erythrocyte is a biconcave disc of a 7 μm diameter and a 2 μm thickness, and blood consists of 45% of the erythrocyte for healthy men and 42% for women in a volume ratio, known as hematocrit. Since the erythrocytes account for 98% of particles in blood, the scattering from blood is mainly attributed to the erythrocytes [15].

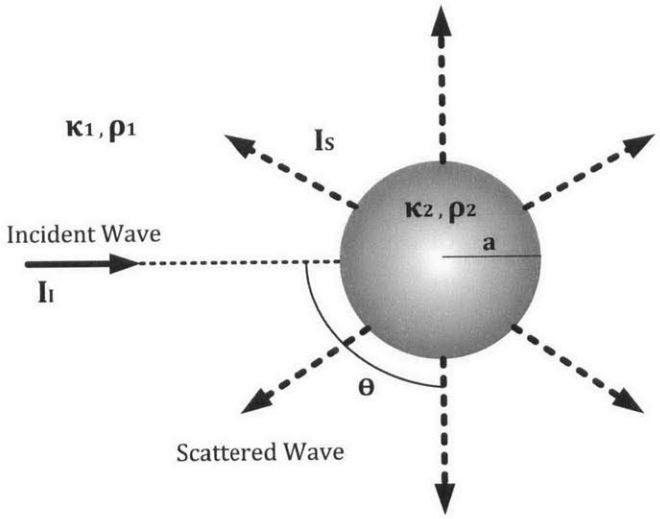

Figure 2-3: Diffusive scattering of a planar incident wave on a spherical object

The diffusive scattering is well analyzed as a Rayleigh scattering. Rayleigh scattering leads to the expression of the intensity of a scattered wave (I_S) from a sub-wavelength spherical object, and its expression is given by [14]

$$\frac{I_S(r)}{I_I} = \frac{16\pi^4 a^6}{9\lambda^4 r^2}[\frac{3(1-\rho_2/\rho_1)\cos\theta}{1+2\rho_2/\rho_1} + (1-\frac{\kappa_1}{\kappa_2})]^2 \tag{2.13}$$

where a is the radius of the object, ρ_i is the density and κ_i is the compressibility in Figure 2-3. In the Rayleigh scattering, the intensity of the scattered acoustic wave depends on the fourth power of the wavelength and the sixth power of the size of the object.

Although Equation 2.13 provides an insight on the diffusive scattering, parame-

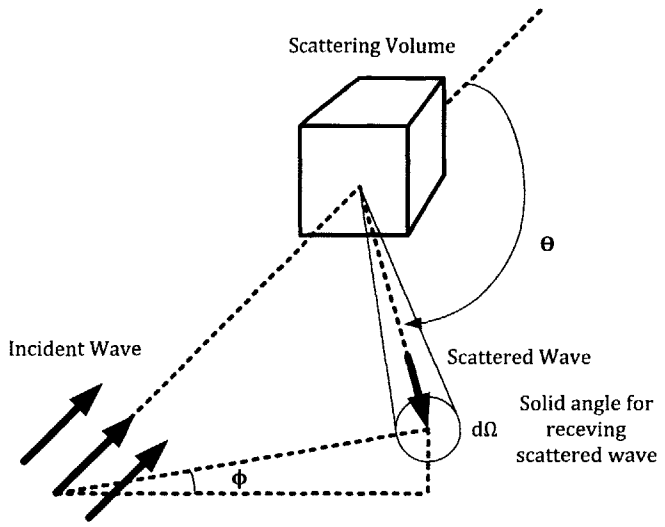

Figure 2-4: Diffusive Scattering of an incident wave on scattering volume from [18]

ters defined from a scattering volume containing numerous scatterers are realistic in describing the acoustic properties of tissue as shown in Figure 2-4. For individual scatterer, a differential scattering cross-section (σ_{ds}) is defined as the ratio of power scattered in particular direction (P_s) to the incident intensity (I) per unit solid angle (Ω), and the cross-section is expressed as following.

$$\sigma_{ds}(\theta, \phi) = \frac{d}{d\Omega} \frac{P_s(\theta, \phi)}{I} \tag{2.14}$$

If the incident wave is scattered from the randomly distributed scatterers, the scattered power is proportional to the number of scatterers. Therefore, a differential scattering coefficient (μ_{ds}) can be expressed as

$$\mu_{ds}(\theta, \phi) = \sum_i n_{si} \sigma_{dsi}(\theta, \phi) \tag{2.15}$$

where σ_{dsi} and n_{si} are the differential scattering cross-section and the number density distribution of individual scatterer types. Particularly, the scattered intensity directly returning to a source such as an ultrasonic transducer is of great importance, and the differential scattering coefficient in this case is denoted as a backscattering coefficient

$\mu_{bs} = \mu_{ds}(\pi, 0)$. A scattering coefficient, then, is defined as the total power scattered in space per unit intensity and per unit scattering volume, and it is given as:

$$\mu_s = \int_0^{4\pi} \mu_{ds}(\theta, \phi) d\Omega \tag{2.16}$$

The backscattering coefficient of blood sample with hematocrit of 26 at 5 MHz is reported around $2 * 10^{-3}/\text{m} \cdot \text{sr}$ [19].

Table 2.2: Relative magnitude of scattered acoustic wave in biological tissues from [16]

Tissue	**Signal Level (dB)**
Fat/muscle (reference*)	0
Placenta	-20
Liver	-30
Kidney	-40
Blood	-60

*reference level taken from typical organ boundary

Diffractive Scattering

For the scatterer and boundary whose roughness is similar to the wavelength, diffractive scattering occurs. In the diffractive scattering, the scattered wave is considered to originate from scatterer surface which acts as a secondary source [14]. The differential scattering cross-section of a spherical object is written as

$$\sigma_s(\theta) = \left[\frac{k^2}{k_s^3}(\gamma_\kappa + \gamma_\rho \cos\theta)(\sin(k_s a) - a k_s \cos(k_s a))\right]^2 \tag{2.17}$$

where $k = \frac{2\pi}{\lambda}$, $k_s = 2k\sin(\frac{\theta}{2})$, $\gamma_\kappa = \frac{\kappa_f - \kappa_a}{\kappa_a}$ and $\gamma_\rho = \frac{\rho_f - \rho_a}{\rho_a}$, and f denotes the small fluctuations from the host material (a). In the diffractive scattering, a scattering pattern shows complicated dependency on a scattering angle (θ), the radius of the scatterer (a) and the wavelength (λ).

2.2 Ultrasonic Transducer Characterization

2.2.1 Piezoelectric Element Physics

An ultrasonic transducer employs a piezoelectric material which converts an electrical signal to a mechanical force and vice versa [18]. For example, lead zirconate titanate (PZT) is commonly used as the piezoelectric material of modern transducer elements. Ceramics and quartz, which are not naturally piezoelectric, are made piezoelectric during their production by placing them into a high electric field at very high temperature [17]. The transducer generates an acoustic wave when excited with an alternating voltage, and the frequency of the transmitted acoustic wave is same as the frequency of the voltage signal. Typically, the frequency of the voltage signal matches to a resonant frequency, which is discussed in the following section, of the piezoelectric element.

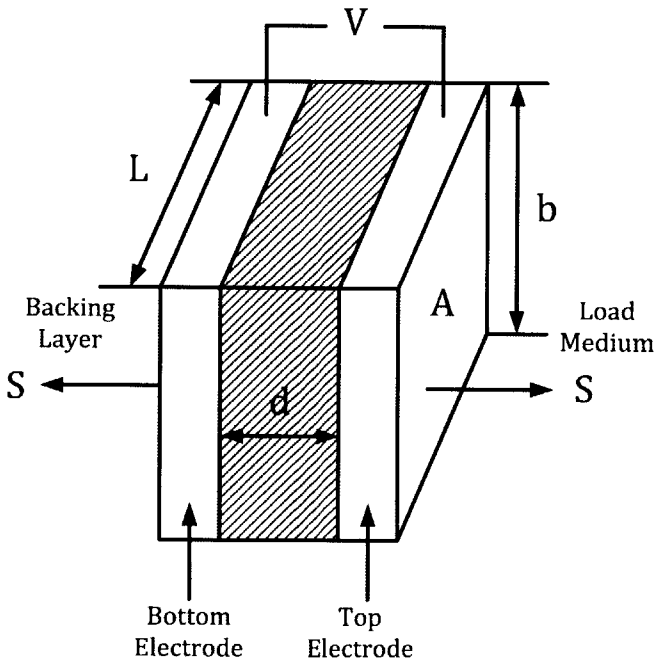

Figure 2-5: Piezoelectric element with parallel electrodes

Figure 2-5 shows a basic piezoelectric element schematic consisting of two electrodes with the cross-sectional area (A), the thickness (d). When a voltage impulse

excites the element through the electrodes, electric charges accumulate in the region near the top and bottom electrode, thus generating stress. This stress is propagated as the acoustic wave across the element. Assuming that the electrodes are thin, and external media have same acoustic impedances, the stress measured at the top electrode shows an impulse followed by a subsequent stress impulse induced at the bottom electrode after a propagation delay, and the stress and its frequency response are expressed as [20]:

$$S(t) = -\frac{hC_0}{2A}(\delta(t) - \delta(t - \frac{d}{c})) \tag{2.18a}$$

$$|S(f)| = \frac{hC_0}{A}|\sin(\frac{\pi f}{2f_0})| \tag{2.18b}$$

where C_0 is the clamped (zero-stress) capacitance, h is the piezoelectric constant, and c is the speed of sound in the piezoelectric element. The frequency response shows resonant frequencies at the odd multiples of a fundamental frequency at $f_0 = \frac{c}{2d}$. The thickness of the element mainly determines the fundamental resonant frequency.

The piezoelectric element is generally regarded as an acoustic resonator including cases when reflection exists due to acoustic impedance mismatch. However, three dimensional nature of the element unavoidably generates multiple resonant modes. For most of the piezoelectric elements, the thickness (d) is far smaller than the width (L) and height (b) of the element. Therefore, other resonant modes are usually negligible [18].

In diagnostic ultrasonography, finer axial resolution (i.e., imaging resolution on a beam axis) is often desirable to identify minuscule tissue structures. A spatial pulse length, determined by both the time duration of the applied voltage pulse and the impulse response of the ultrasonic transducer, sets the axial resolution of imaging systems. In order to achieve a short impulse response, a damping material is usually placed in a backing layer at the cost of reduced efficiency of the transducer. The quality factor (Q-factor) is defined as the reciprocal of the fractional bandwidth of the pulse. For short pulses, the Q-factor is approximately coincides with the number of cycles in the pulse, and the insertion of the damping material lowers the Q-factor at the same voltage excitation, achieving the finer axial resolution [17].

Unlike the previous assumption, the acoustic impedances of the piezoelectric materials differ significantly from load medium (e.g., water, tissue). As a consequence, only fractional acoustic power is transmitted to the load medium. In order to reduce the reflection of the acoustic wave during both a transmit and a receive, a series of matching layers which have intermediate acoustic impedances is inserted to enhance overall acoustic coupling. The optimal thickness of this matching layer is a quarter wavelength [17].

2.2.2 Equivalent Circuit Model

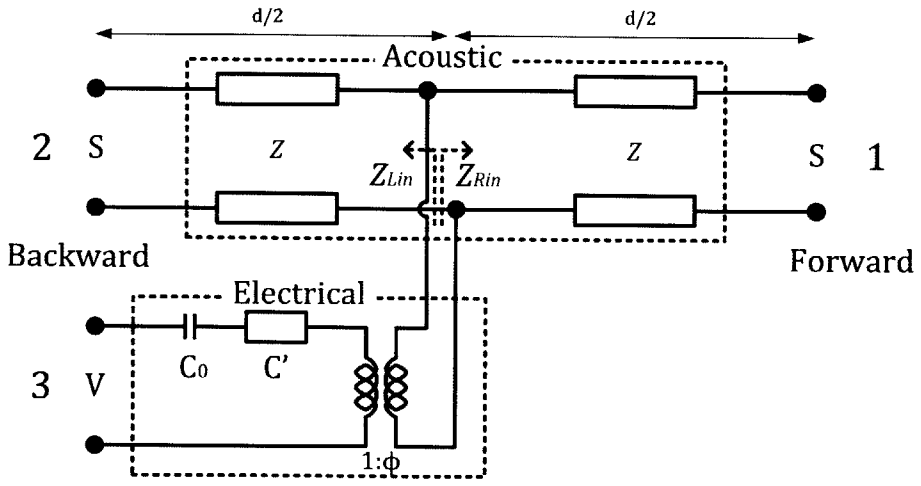

Figure 2-6: KLM equivalent circuit model for a piezoelectric element

To the first order, the piezoelectric element is modeled into an equivalent electrical circuit. Mason model [21] utilizes an analogy between acoustical parameters (e.g., stress (S) or force and a particle velocity) and electrical parameters (e.g., a voltage and a current) to derive several models for different piezoelectric transducer geometries [14]. A KLM model, introduced by Krimholtz, Leedom, and Matthaei [22], is especially useful when only one dominant resonant mode exists, which is a thickness-expander mode in medical ultrasound transducers. The advantage of the KLM model is to separate the acoustic and electrical parts of transduction process through a transformer shown in Figure 2-6. In addition, the KLM model is especially useful for a

broadband transducer design [23].

The KLM model shown in Figure 2-6 consists of two acoustic ports and one electric port. The port one leads to the matching layer and the load medium where the acoustic wave propagates. The port two reaches the backing layer. In the KLM model, an artificial acoustic center is created for convenience of analysis even though the stress of the piezoelectric material is induced at the boundaries of the element [18]. In the acoustic domain, an acoustic transmission line accounts for the propagation and resonant behavior of the piezoelectric element. The acoustic transmission line is characterized by the thickness (d), the speed of sound in piezoelectric material (c), and the acoustic impedance (Z). The electrical signal is transformed into the acoustic domain through the transformer with the turns ratio of $1 : \phi$. The electrical domain of the KLM model consists of the clamped capacitance (C_0) and a negative capacitance-like component (C') which models an acoustoelectric feedback. The turns ratio (ϕ) and C' is expressed as [14] :

$$\phi = k_T(\frac{\pi}{\omega_0 C_0 Z_C})^{\frac{1}{2}} sinc(\frac{\omega}{2\omega_0}) \tag{2.19}$$

$$C' = -\frac{C_0}{k_T^2 sinc(\frac{\omega}{\omega_0})} \tag{2.20}$$

where k_T is an electromechnical coupling constant. The electrical input impedance of a loaded transducer provides insight into a driver and receiver design. For simplicity of analysis, only the port one is loaded. Then, the electrical input impedance from port three is given as [23]

$$Z_T(\omega) = \frac{1}{j\omega C_0} + Z_a = \frac{1}{j\omega C_0} + R_a + jX_a \tag{2.21a}$$

$$R_a = \frac{k_T^2}{\pi\omega_0 C_0}(\frac{\omega_0}{\omega})^2(1 - \cos(\frac{\pi\omega}{\omega_0}))^2 \tag{2.21b}$$

$$X_a = \frac{2k_T^2}{\pi\omega_0 C_0}(\frac{\omega_0}{\omega})^2 \sin\frac{\pi\omega}{\omega_0}(1 - \frac{1}{2}\cos(\frac{\pi\omega}{\omega_0})) \tag{2.21c}$$

where Z_a is denoted as a complex acoustic radiation impedance. It is worth noting

that the complex acoustic radiation impedance becomes purely real at the resonant frequency. However, due to non-ideality, a matching network (such as a series inductor) at the electrical port may be inserted to compensate for a capacitive input impedance to minimize power loss from the large capacitive load.

2.2.3 Pressure Field in Continuous Wave

The acoustic wave induced from the piezoelectric element propagates through the load medium from the surface of an ultrasonic transducer. The acoustic wave radiating from a finite aperture is considered equivalently as many infinitesimal sources on the aperture radiating spherical waves according to the Huygens' principle [14]. Hence, many spherical waves interfere with each other in both constructively and destructively, and this phenomenon results in a specific pattern, known as a diffraction pattern. Especially, the diffraction pattern becomes distinct as the dimension of the aperture reaches the wavelength of the radiating wave. In fact, the aperture size of medical ultrasonic transducers (few mm scale) is close to the wavelength of the medical ultrasound (hundreds of μm). Therefore, diffraction explains the detailed acoustic beam pattern in medical ultrasound.

A pressure field amplitude in Figure 2-7 is written in terms of a spatial integral over the transducer surface to add contributions from each of point sources as [14]

$$p(\vec{r},t) = \frac{j\rho_0 ckv_0}{2\pi}\int_S \frac{e^{i[\omega t - k(\vec{r}-\vec{r_0})]}}{|\vec{r}-\vec{r_0}|}A(\vec{r_0})dS \tag{2.22}$$

where ρ_0 is the density of the medium, $v_0 A(\vec{r_0})$ is the velocity normal to the surface, c is the speed of sound and k is the wavenumber. Equation 2.22 is also called the Rayleigh-Sommerfeld integral [14]. In the region where $\frac{|x-x_0|}{z}, \frac{|y-y_0|}{z} \ll 1$, $|\vec{r}-\vec{r_0}|$ is expanded by applying a parabolic approximation (Fresnel approximation) as:

$$|\vec{r}-\vec{r_0}| = \sqrt{z^2+(x-x_0)^2+(y-y_0)^2} \simeq z[1+\frac{1}{2}(\frac{x-x_0}{z})^2+\frac{1}{2}(\frac{y-y_0}{z})^2] \tag{2.23}$$

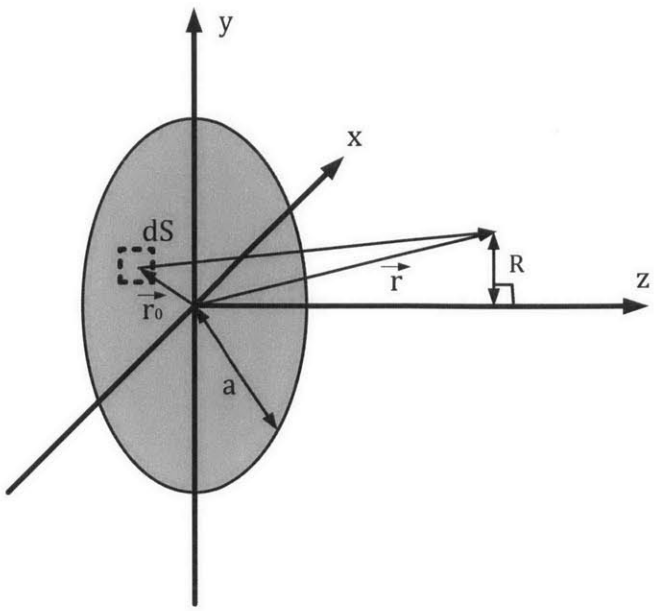

Figure 2-7: Geometric representation of a transducer aperture and its coordinates

Plugging Equation 2.23 into Equation 2.22 results in:

$$p(\vec{r},t) = \frac{j\rho_0 ckv_0}{2\pi z} e^{i(\omega t - kz)} e^{-ik(x^2+y^2)/2z} \iint_S [e^{-ik(x_0^2+y_0^2)/2z} A(x_0,y_0)] e^{ik(xx_0+yy_0)/z} dx_0 dy_0 \tag{2.24}$$

Equation 2.24 shows that the beam pattern at the fixed depth (z) is the spatial Fourier transform of $e^{-ik(x_0^2+y_0^2)/2z}A(x_0,y_0)$. This diffraction pattern is defined as the Fresnel diffraction. As $z > x_0^2 + y_0^2$, then the Fresnel diffraction pattern is further approximated into the Fraunhofer diffraction which states that the beam pattern at the fixed depth is just the spatial Fourier transform of the aperture itself.

Equation 2.24 can be applied to an arbitrary aperture, and analytic solutions for simple geometries (e.g., rectangular or circular) are already presented. Especially, many single element transducers have the circular aperture, and the pressure field in the Fraunhofer region (far-field) of the circular aperture is given as [14]:

$$p(R,z,\lambda) = \frac{jp_0\pi a^2}{\lambda z} \frac{2J_1(2\pi Ra/\lambda z)}{2\pi Ra/\lambda z} \tag{2.25}$$

where J_1 is the first order Bessel function, and a is the radius of the circular aperture. A beam width is defined as a distance between two points where the pressure amplitude drops to a half of maximum. The FWHM (Full Width Half Maximum) beam width is expressed as:

$$FWHM = 0.7047\frac{\lambda z}{a} \tag{2.26}$$

The pressure amplitude on a z-axis is expressed as:

$$|p(0, z, \lambda)| = 2p_0 \sin[\frac{kz}{2}(\sqrt{1 + (a/z)^2} - 1)] \tag{2.27}$$

and a near-to-far field transition depth (z_r), also known as the natural focus, occurs at:

$$z_r = \frac{a^2}{\lambda} \tag{2.28}$$

Equation 2.28 shows the natural focus is only relevant to the aperture radius (a) and the wavelength of the acoustic wave (λ). Figure 2-8 presents continuous pressure fields in both a radial and an axial dimension. Most of the acoustic energy is concentrated within the beam width. In the axial dimension, the pressure amplitude shows many notches in a near-field while the pressure amplitude monotonically decreases in the

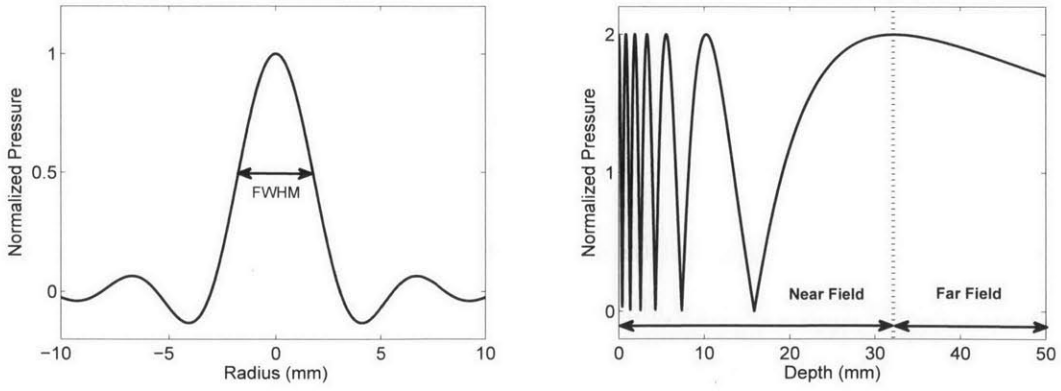

(a) Radial Dimension Pattern at z_r

(b) Axial Dimension Pattern

Figure 2-8: Simulated continuous pressure in a radial axial dimension for a circular aperture of 5 mm radius at continuous 2 MHz ultrasound

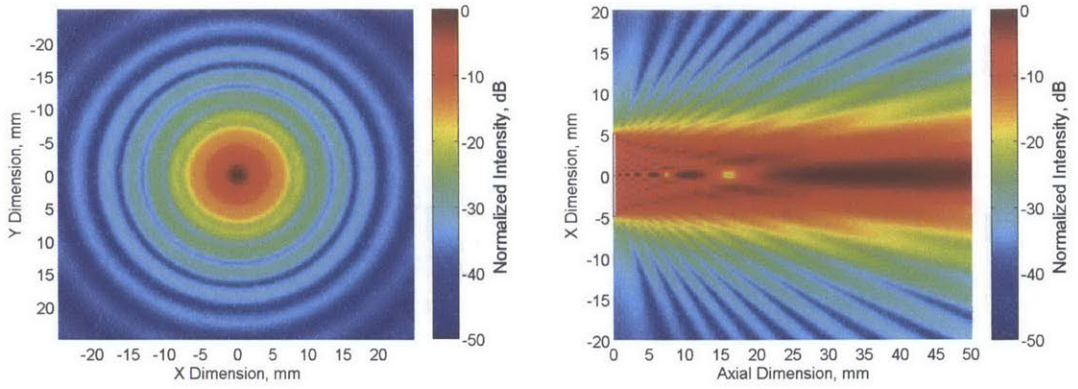

(a) $x - y$ plane (b) $x - z$ plane

Figure 2-9: Simulated continuous pressure a temporal-averaged intensity field in $x-z$ and $x - y$ plane for a circular aperture of 5 mm radius at 2 MHz ultrasound

far field. Figure 2-9 shows the continuous pressure field amplitude in $x - z$ and $x - y$ plane.

In ultrasonic imaging systems, the beam width determines the lateral resolution of images, thereby requiring a higher operation frequency and a larger aperture for finer lateral resolution. In addition, modern medical ultrasound utilizes a phased array transducer in order to enhance focusing capability, adjust a focal depth and achieve beam steerability. Since the natural focus is the point where significant constructive interference occurs at last, the focal depth adjustment is only achieved within the near-field region.

2.2.4 Pressure Field in Pulsed Wave

Most of medical ultrasonography is operated in a pulsed manner because the pulsed operation eliminates the ambiguity of depth information. Therefore, an operator can target and obtain physiological information at the specific region of interest. Although the analysis of the continuous pressure field provides a great insight on the diffraction beam pattern, the analysis does not include the exact temporal behavior of a pulsed pressure field. This section briefly describes two powerful techniques for a pulsed pressure field analysis.

From the more general Rayleigh integral, a pressure field description for both continuous and pulsed wave is given based on Huygens' principle again as [15]:

$$\begin{aligned} p(\vec{r},t) &= \frac{\rho_0}{2\pi}\int_S \frac{\partial v_n(\vec{r_0}, t-\frac{|\vec{r}-\vec{r_0}|}{c})/\partial t}{|\vec{r}-\vec{r_0}|}dS \\ &= \rho_0 v_n(t) * \frac{\partial}{\partial t}\int_S \frac{\delta(t-\frac{|\vec{r_0}-\vec{r}|}{c})}{2\pi|\vec{r}-\vec{r_0}|}dS \\ &= \rho_0 v_n(t) * \frac{\partial h(\vec{r},t)}{\partial t} \end{aligned} \tag{2.29}$$

where $h(\vec{r},t)$ is defined as a spatial impulse response [15]. Equation 2.29 allows to obtain a time domain pressure waveform in space if the spatial impulse response is known. Since the geometry of the aperture determines the spatial impulse response, Equation 2.29 is easily utilized to depict the pressure field waveform for any acoustic waves [15]. The other powerful technique is based on the reciprocity theorem of acoustics, which states a transmitter and a receiver are interchangeable [15]. The implication of the reciprocity theorem is the spatial impulse response is reconstructed by observing the transducer's response to a point source in space radiating a spherical wave. Then, the pulsed pressure field can be obtained similarly using the spatial impulse response as given by Equation 2.29. Figure 2-10 shows the pulsed pressure field amplitude in a $x-z$ and a $x-y$ plane. The pressure field patterns of the continuous (Figure 2-9) and pulsed (Figure 2-10) wave show similarity while the pulsed beam pattern is much smoother in space. Though Equation 2.26 and 2.28 are useful, an acoustic simulator, such as Field II, provides the exact beamwidth and the natural focus of a given aperture in the pulsed ultrasound.

Finally, a received pressure response (p_r) is expressed in terms of a spatial inhomogeneity (f_m) and a pulse-echo impulse response (v_{pe}), including both a transducer excitation and an electromechanical impulse response, written as [15]:

$$p_r(\vec{r},t) = v_{pe}(t) *_t f_m(\vec{r}) *_r h_{pe}(\vec{r},t) \tag{2.30}$$

where $*_t, *_r$ are denoted as a temporal convolution and a spatial convolution, re-

spectively. Additionally, $h_{pe}(\vec{r}, t)$ accounts for the spatial impulse response for both transmit and receive.

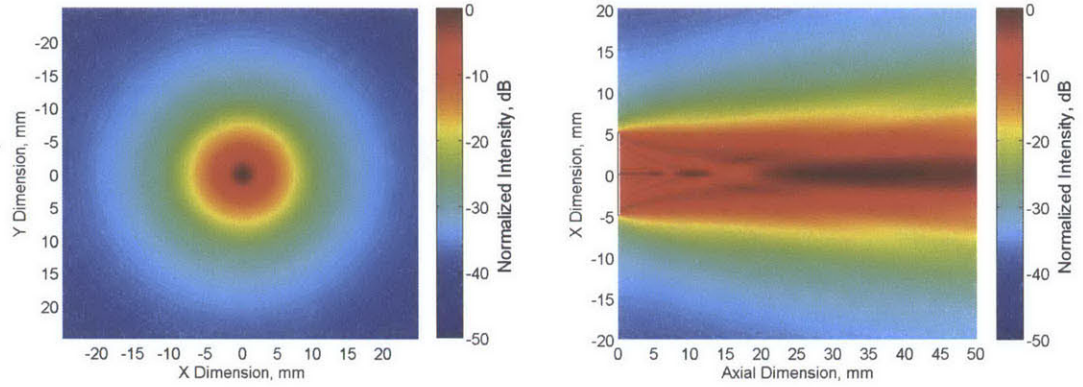

(a) $x - y$ plane

(b) $x - z$ plane

Figure 2-10: Simulated pulsed pressure a temporal-averaged intensity field in $x - z$ and $x - y$ plane for a circular aperture of 5 mm radius at 3 cycles of 2 MHz ultrasound

Chapter 3

Hemodynamics of Arterial System

The circulatory system provides various organs and tissues with oxygen and nutrition which are essential to metabolism, and the system disposes carbon dioxide and wastes as well. Especially, arterial blood delivers oxygen and nutrition, and its flow is driven by arterial blood pressure (ABP) exerted by the contraction of the left ventricle. Although this simplistic view explains the main role of the heart in the circulatory system, the relationship between the blood flow and the pressure is very complicated and also highly dependent on the mechanics of vascular structures. This chapter begins to focuses on the basic hemodynamics of the arterial system. Thereafter, it introduces the anatomical background of the arterial system.

3.1 Blood Flow Physics

This section introduces basic flow physics assuming a blood vessel is modeled as a cylindrical tube. It begins with the analysis of constant flow followed by pulsatile flow. Typically, the comprehensive description of flow dynamics requires the solution of the Navier-Stokes equation [15], but this section mainly stays within a simple view to provide the clear idea of blood flow physics.

3.1.1 Steady Flow

First of all, fluid is assumed incompressible in macro-scale although the existence of a longitudinal acoustic wave in the fluid acknowledges localized compression. This incompressibility implies a constant volumetric flow rate (Q) along an entire rigid tube as given by [15]:

$$Q = A\bar{v} = A_1\bar{v_1} = A_2\bar{v_2} \tag{3.1}$$

where $\bar{v}$ is the average flow velocity over the cross-section of the tube.

In addition, the mechanical energy (kinetic, potential and internal energy) of the fluid must be conserved, and the description of energy conservation is represented in Bernoulli's equation as [15]:

$$\frac{p_1}{\rho_1} + \frac{v_1^2}{2} + gh_1 + U_1 = \frac{p_2}{\rho_2} + \frac{v_2^2}{2} + gh_2 + U_2 \tag{3.2}$$

where g is gravitational acceleration, p is the pressure, ρ is the density, v is the flow velocity, and U is denoted as internal energy per unit mass. In the human body, blood's density and temperature are almost constant, so its internal energy change is negligible. Therefore, Equation 3.2 somewhat relates the flow velocity and the pressure measured at different height representing different arterial sites.

Another important property of fluid is viscosity originated from shear stress between layers of fluid each of which moves at different velocity. The viscosity (μ) is defined as the proportionality between the sheer stress and strain as Equation 3.3a and more generally Equation 3.3b:

$$\frac{dF}{dA} = \mu\frac{dv}{dy} \tag{3.3a}$$

$$S_{xy} = \mu(\frac{dv}{dy} + \frac{du}{dx}) \tag{3.3b}$$

where S_{xy} is the sheer stress, and v, u are the velocities in x and y direction, respectively. Figure 3-1 shows the sheer stress between the fluid layers of the different flow velocities. For ideal fluid, called Newtonian fluid, the viscosity is independent of

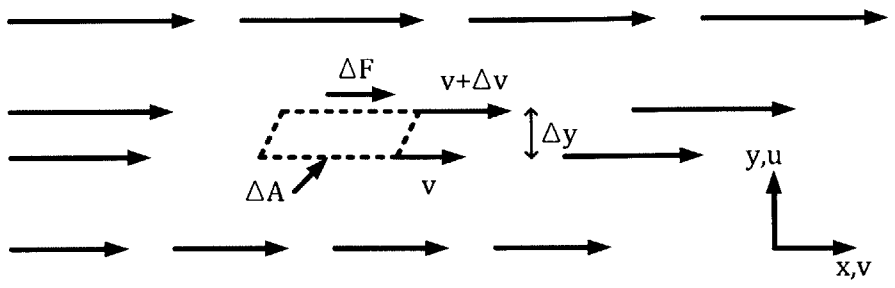

Figure 3-1: Illustration of force on small fluid volume in a rigid tube from [15]

sheer stress. However, blood is a complex fluid which is described as the suspension of blood cells and plasma, and the viscosity of the blood changes with the sheer stress. The viscosity of the blood is also dependent on temperature and hematocrit. Still, given that the hematocrit of human is well controlled between 42–45%, and the body temperature is well regulated to 36.5°C, the viscosity of the blood is often assumed to be 4×10^{-3} kg/m · s [15].

Because of the viscosity of the fluid and the friction from the tube's wall, a velocity profile develops to balance the sheer stress with a driving force. In constant laminar flow (i.e., fluids flowing in parallel), the velocity profile eventually becomes parabolic and its profile is expressed as:

$$v(r) = v_{max}\left(1 - \left(\frac{r}{R}\right)^2\right) \tag{3.4}$$

where r is the radius from the axis, v_{max} is the maximum velocity, and R is the inner radius of the tube [15]. When the velocity profile becomes parabolic, a viscous drag force at every laminae is balanced against the driving force originated from a pressure gradient, thus maintaining a constant flow velocity at every laminae. The parabolic profile usually develops after the fluid passes through a long rigid tube.

In the vascular system, the blood vessels often branch into smaller vessels, and the velocity profile at the entrance of small branches shows a transient profile other than the parabolic profile. When the branching vessel is significantly smaller, the velocity profile at the entrance is almost flat, known as a plug profile. The velocity

profile gradually changes from the plug to eventually the parabolic profile as the blood experiences the viscous drag while flowing downstream. This transient velocity profile is often described by Poiseuille flow profile given as:

$$v(r) = v_{max}\left(1 - (\frac{r}{R})^{p_0}\right) \tag{3.5}$$

where p_0 is a Poiseuille coefficient. The poiseuille coefficient varies from infinite (plug profile) to two (parabolic profile). The average velocity over the cross-section, defined as a spatial mean velocity, for Poiseuille flow is given as:

$$\bar{v} = \frac{1}{\pi R^2}\int_0^R v_{max}\left(1 - (\frac{r}{R})^{p_0}\right) \times 2\pi r dr = v_{max}\frac{p_0}{p_0 + 2} \tag{3.6}$$

In the parabolic profile, the spatial mean velocity is exactly a half of the maximum velocity (v_{max}). In addition, the phenomenon of having the non-parabolic velocity profile is called an entrance effect, and the distance from the entrance to the point having the parabolic profile is known as an inlet length. The inlet length is dependent on the tube's dimension, the viscosity, density of the fluid and the spatial mean velocity [15].

The viscous drag requires an external force on the fluid to maintain a constant flow rate, and the pressure gradient along the tube acts as the driving force against the viscous drag. Then, the viscous resistance (R_f) in the parabolic profile is given by

$$\Delta P = R_f Q = \frac{8\mu L}{\pi R^4}Q \tag{3.7}$$

where ΔP is the pressure difference between the inlet and outlet of the tube, Q is the volumetric flow rate, and L is the length of the tube. As seen in Equation 3.7, the viscous resistance is inversely proportional to the fourth power of the tube's radius.

3.1.2 Pulsatile Flow

The description of pulsatile flow is not as straightforward as that of steady flow, but the analysis based on the approximation of the Navier-Stokes equations is sufficient

to interpret the overall behavior of pulsatile flow. The Navier-Stokes equations are given as [24]:

$$-\frac{dP}{dx} = \rho(\frac{dv}{dt} + u\frac{dv}{dr} + v\frac{dv}{dx}) - \mu(\frac{d^2v}{dr^2} + \frac{1}{r}\frac{dv}{dr} + \frac{d^2v}{dx^2}) \tag{3.8a}$$

$$-\frac{dP}{dr} = \rho(\frac{du}{dt} + u\frac{du}{dr} + v\frac{du}{dx}) - \mu(\frac{d^2u}{dr^2} + \frac{1}{r}\frac{du}{dr} + \frac{d^2u}{dx^2} - \frac{u}{r^2}) \tag{3.8b}$$

where v is a longitudinal velocity and u is a radial velocity. Equation 3.8a and 3.8b describe a longitudinal pressure gradient and a radial pressure gradient, respectively. The terms associated with the density (ρ) represents inertial nature of the fluid while the terms associated with the viscosity (μ) represents viscous nature. The general solution of the Navier-Stokes equation does not exist, but analytic solutions by neglecting the non-linear terms and assuming laminar flow are obtainable [24].

Womersley's analysis of pulsatile flow gives a complete analytic solution within these assumptions and is described in a series of papers [25, 26]. The analysis begins with neglecting non-linear terms in Equation 3.8a as [24]:

$$-\frac{dP}{dx} = \rho(\frac{dv}{dt}) - \mu(\frac{d^2v}{dr^2} + \frac{1}{r}\frac{dv}{dr}) \tag{3.9}$$

The analysis further assumes that the pressure gradient is only a function of time, which is true for the rigid tube, and the pressure gradient is written as $|A|\cos(\omega t)$. Then, the longitudinal velocity (v) and the volumetric flow rate (Q) are expressed as:

$$v(r,t) = Real[\frac{|A|e^{j\omega t}R^2}{j\alpha^2\mu}(1 - \frac{J_0(j^{3/2}\alpha\frac{r}{R})}{J_0(j^{3/2}\alpha)})] \tag{3.10}$$

$$Q(t) = \frac{|A|\pi R^4}{\mu} \cdot \frac{M'_{10}}{\alpha^2}\cos(\omega t - \phi - [90^\circ - \epsilon'_{10}]) \qquad (M'_{10}e^{j\epsilon'_{10}} = 1 - \frac{2J_1(j^{3/2}\alpha)}{j^{3/2}\alpha J_0(j^{3/2}\alpha)}) \tag{3.11}$$

where α is defined as the Womersley number ($\alpha = R\sqrt{\frac{\rho}{\mu}w}$). The Poiseuille's flow model shows that the velocity profile varies as the fluid travels downstream while the Womersley's pulsatile flow model further shows that the velocity profile driven

by the oscillatory pressure gradient ($|A|\cos(\omega t)$) is time-varying. Figure 3-2 shows a time-varying velocity profile in the Womersley's pulsatile flow model. The analytic solution for an elastic tube, which is a more realistic model for the arterial vessels, also exists in a similar form of Equation 3.10, 3.11, and is referred to [24].

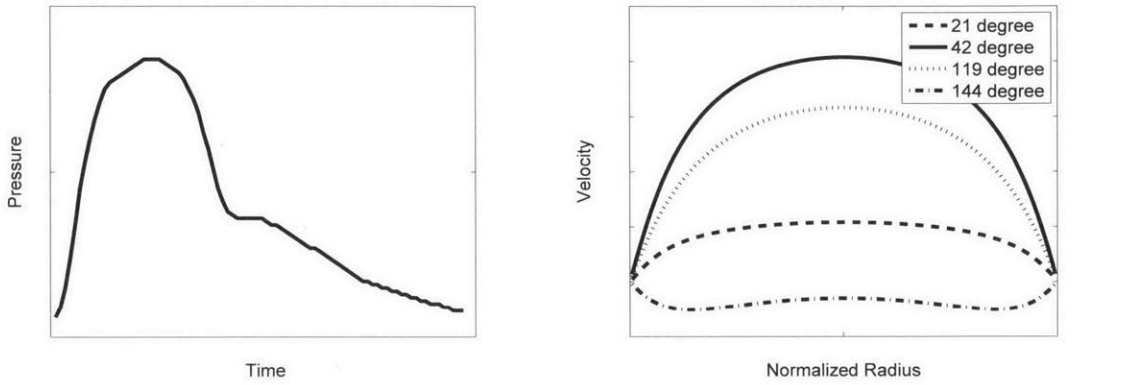

(a) ABP waveform in a cardiac cycle (b) Velocity profile variation over a cardiac cycle

Figure 3-2: Illustration of Womersley's pulsatile velocity profile in different cardiac phases

3.2 Pulse Pressure Wave

The arterial blood vessels have viscoelastic properties to withstand high blood pressure and to buffer the surge of blood pressure caused by the contraction of the left ventricle. Therefore, a simple elastic tube often models the arteries. While the analysis of flow physics in the rigid tube is derived based on a given pressure gradient as a sole driving force, the analysis in the elastic tube introduces the other aspect that a flow gradient drives a pressure increase as well. This aspect implies the distinct wave propagation mode of pressure and flow. It is noteworthy that this pressure wave is completely different from a longitudinal acoustic wave and only exists within the elastic tube filled with fluid. This pressure wave is known as a pulse pressure wave which is caused by the pulsatile change of the pressure. The following section describes the nature of this phenomenon.

3.2.1 Pulse Pressure Wave Propagation

First of all, it is assumed that the viscous drag is negligible. This assumption is reasonable in major arteries which have large vessel cross-section, implying a small viscous resistance. In addition, the assumption also holds when the pressure gradient is steep to cause high acceleration of the blood, implying the inertial terms dominate the viscous terms in the Navier-Stokes equation. Then, Equation 3.9 is further simplified as the following [24]:

$$-\frac{dP}{dx} = \frac{\rho}{A}(\frac{Adv}{dt}) = \frac{\rho}{A}(\frac{dQ}{dt}) \tag{3.12}$$

Equation 3.12 simply means the pressure gradient accelerates the fluid.

If the pressure gradient is also the function of a longitudinal dimension, the acceleration of the fluid is also the function of a longitudinal dimension, thus causing the flow gradient. Since the fluid is assumed Newtonian fluid (i.e., non-compressible), the consequence of the flow gradient is the change of the cross-sectional area by radially expanding the elastic tube with the pressure, and it is expressed in a continuity equation as:

$$-\frac{dQ}{dx} = \frac{dA}{dt} = \frac{dA}{dP}\frac{dP}{dt} \tag{3.13}$$

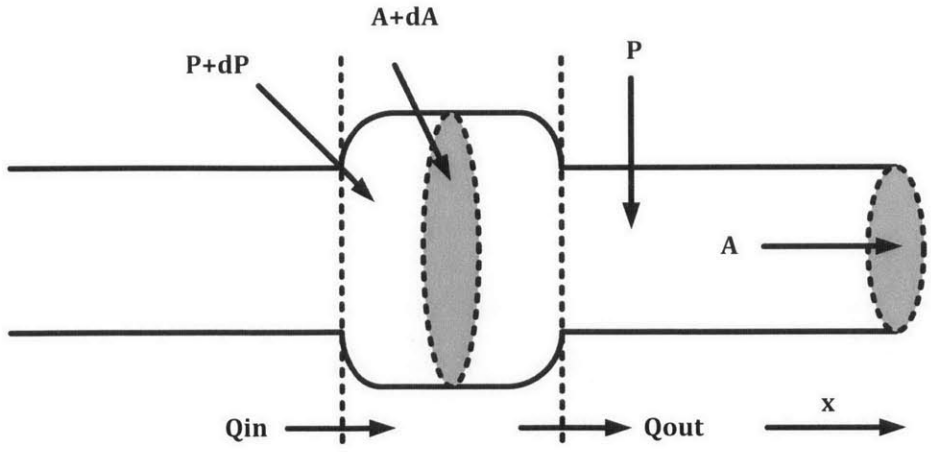

Figure 3-3: Schematic of an elastic tube

Table 3.1: Analogy of pulse pressure propagation in elastic tube to transmission line

Elastic Tube	**Transmission Line**
Pressure (P)	Voltage (V)
Flow (Q)	Current (I)
Inertia ($\frac{\rho}{A}$)	Unit length inductance (L)
Compliance ($\frac{dA}{dP}$)	Unit length capacitance (C)

where $\frac{dA}{dP}$ is defined as the compliance of the tube. Because of the elasticity, the tube is able to dilate or contract in response to internal pressure change such that its hoop tension matches the pressure difference between inside and outside of the tube. Figure 3-3 shows the schematic of the elastic tube in the pulsatile flow. Equation 3.12 and 3.13 resemble fundamental equations in a transmission line theory where P and Q are corresponding to voltage (V) and current (I), respectively. Table 3.1 summarizes the analogy between the elastic tube and the transmission line.

As an electromagnetic wave propagates in the transmission line, a time varying pressure applied at the inlet of the tube propagates. In the arterial system, the contraction of the left ventricle causes the time varying blood pressure propagating along the arteries. The phase velocity of the propagating pulse pressure wave is given by the Bramwell-Hill equation [24]:

$$PWV = \sqrt{\frac{A}{\rho}\frac{dP}{dA}} \tag{3.14}$$

where the phase velocity is called a pulse wave velocity (PWV). It is noteworthy that the PWV is clearly a different parameter from the flow velocity. While the flow velocity is the velocity of fluid movement in the tube, the PWV is the phase velocity of the pulse pressure wave which is closely related to the compliance ($\frac{dA}{dP}$) of the tube as seen in Equation 3.14. The Bramwell-Hill equation is further simplified to the Moens-Korteweg equation if the elastic tube has a thin wall, and the equation is

written as:

$$PWV = \sqrt{\frac{Eh}{2\rho R}} \tag{3.15}$$

where E is the Young's modulus, and h is the thickness of the tube [24].

In reality, however, various energy loss mechanisms attenuate the amplitude of the pulse pressure wave. First, the viscous drag weakens energy associated with the flow. Second, the viscoelastic nature of the arterial vessel wall causes energy dissipation of the pulse pressure wave while the vessel dilates and contracts. Nonetheless, as long as energy loss mechanisms are relatively insignificant, the propagation of the pulse pressure wave is validly modeled with the same PWV in Equation 3.14 and a simple attenuation model.

3.2.2 Pulse Pressure Wave Reflection

In hemodynamics, vascular impedances describe the relations between the blood pressure and the blood flow, and there are three types of vascular impedance, expressed as:

$$Z_L = \frac{-dP/dx}{Q} \tag{3.16}$$

$$Z_c = \frac{dP}{dQ} \tag{3.17}$$

$$Z_W = \frac{P}{-dQ/dx} \tag{3.18}$$

where Z_L is a longitudinal impedance, Z_c is a characteristic impedance, and Z_W is a transverse impedance [24]. The viscous resistance is a kind of the longitudinal impedance in a rigid tube with constant flow. The characteristic impedance is the ratio of the pressure to the flow in a forward traveling wave, and it is same as an input impedance ($Z_I = \frac{P}{Q}$) during a reflection-free period. The characteristic impedance is written in terms of the compliance and the inertial term as:

$$Z_c = \sqrt{\frac{\rho}{A}\frac{dP}{dA}} \tag{3.19}$$

Similar to the electromagnetic wave propagation in the transmission line, the reflection of the pulse pressure and the flow wave occurs where the characteristic impedances do not match. Equation 3.19 implies that the characteristic impedance varies if the compliance or the cross-sectional area of the vessel changes. The reflection coefficient (Γ) is defined as the ratio of an incident to a reflected pulse pressure wave, expressed as:

$$\Gamma = \frac{Z_2 - Z_1}{Z_2 + Z_1} \tag{3.20}$$

where Z_1 and Z_2 are the characteristic impedances, and the pulse pressure propagates from medium 1 to 2. Therefore, if the pulse pressure wave propagates into a high terminal impedance (high Z_2) such as the vascular impedance of arterioles, a strong reflection occurs.

Considering that the PWV is several m/s and the strong reflection occurs at the

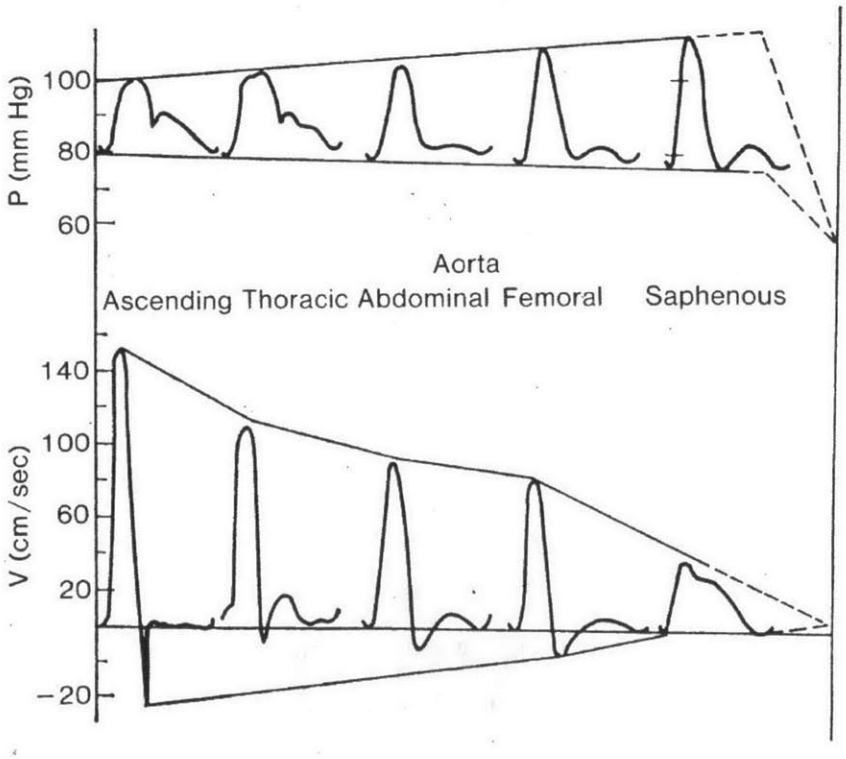

Figure 3-4: Pressure (above) and blood flow velocity (below) of arteries in a dog from [24]

peripheral arterioles [24, 27], an observed arterial blood pressure (ABP) waveform is certainly the result of superposition of the forward and the backward traveling wave due to the reflection. Therefore, the shape of the ABP waveform measured at various sites varies significantly depending on the distance between a measurement site to a reflection site. Figure 3-4 presents the ABP waveform measured at different arterial sites. This figure clearly shows that a pulse pressure (i.e., difference between systolic and diastolic pressure) increases as the observation site approaches to the periphery. This phenomenon is mainly attributed to the strong reflection at the peripheral site, which adds up an extra pulse pressure on top of the forward traveling pressure wave in a more aligned manner at the peripheral measurement sites (e.g., a saphenous artery).

3.3 Anatomical and Physiological Background of Arterial System

The vascular system consists of arteries, capillaries and veins. The arterial system mostly provides oxygenated blood to organs and tissues except a pulmonary artery, which is a pathway to supply deoxygenated blood for gas exchange at the lung. This section concentrates on the anatomy of an arterial tree (i.e., major arteries and associated branches).

Figure 3-5 provides the overview of major arteries at the upper body. The arterial tree starts at the left ventricle of the heart where the blood pressure driving circulation is generated. The left ventricle is connected to the ascending aorta, through the aortic valve, and the coronary artery branches out. Three main branches spread out from the aortic arch. The first artery is the right brachiocephalic trunk which leads to the subclavian artery, the brachial artery (BA), the radial and the ulnar artery. The right common carotid artery is also branched from the right brachiocephalic trunk. The second artery is the left common carotid artery which directly branches out from the aortic arch unlike the right common carotid artery. The last one is

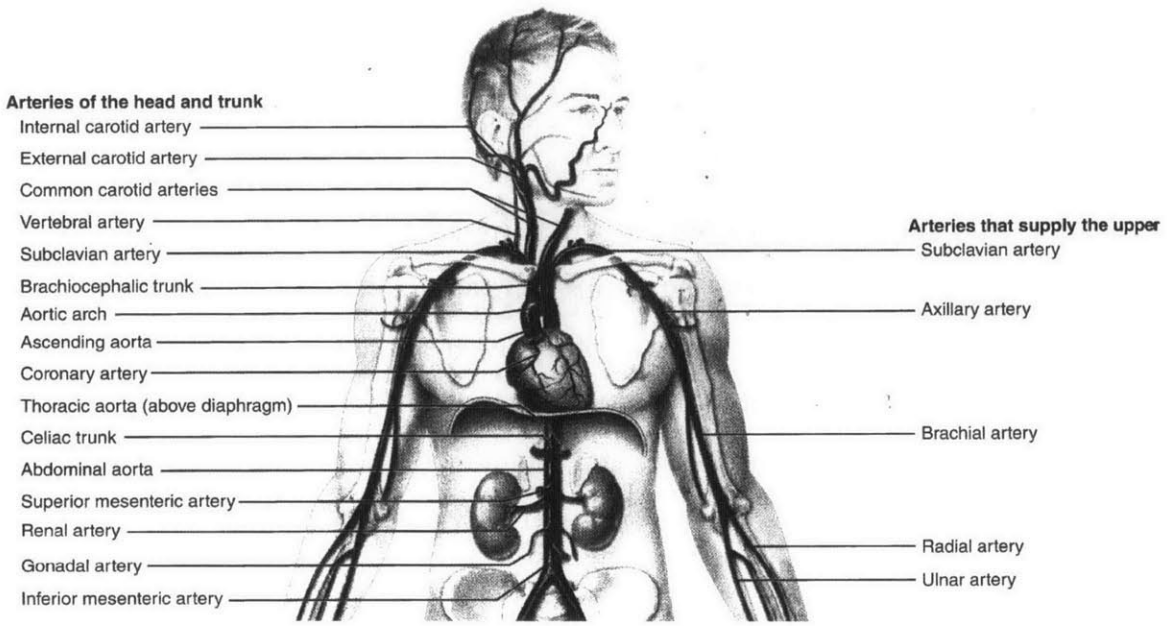

Figure 3-5: Illustration of vascular structures in upper body from [28]

the left subclavian artery. The subclavian artery is the main pathway to supply blood in upper extremities. At the downstream of the subclavian artery, the brachial artery is located where a sphygmomanometer measures systolic and diastolic blood pressure. The common carotid artery (CCA) is the main artery to supply blood into the head and brain. At the downstream of the CCA, the internal and external common carotid artery are bifurcated. Both of the CCA and the BA are superficial and easily accessible among major arteries.

As the arteries branch out, they become successively smaller, thus resulting in the change of the characteristic impedance. Eventually, the arterioles which connect the major arteries to the capillaries have very narrow cross-section, thus having a high vascular impedance. Because of its high vascular impedance, most of the ABP drops at the arterioles, and a systemic vascular impedance is dominated by the arterioles'. In addition, because of the significant characteristic impedance mismatch at the arterioles, the strong wave reflection occurs. One of the important functionalities of the arterioles is to regulate the blood flow and the blood pressure. The arteriole is responsive to the autonomic nervous system and circulatory hormones in order to

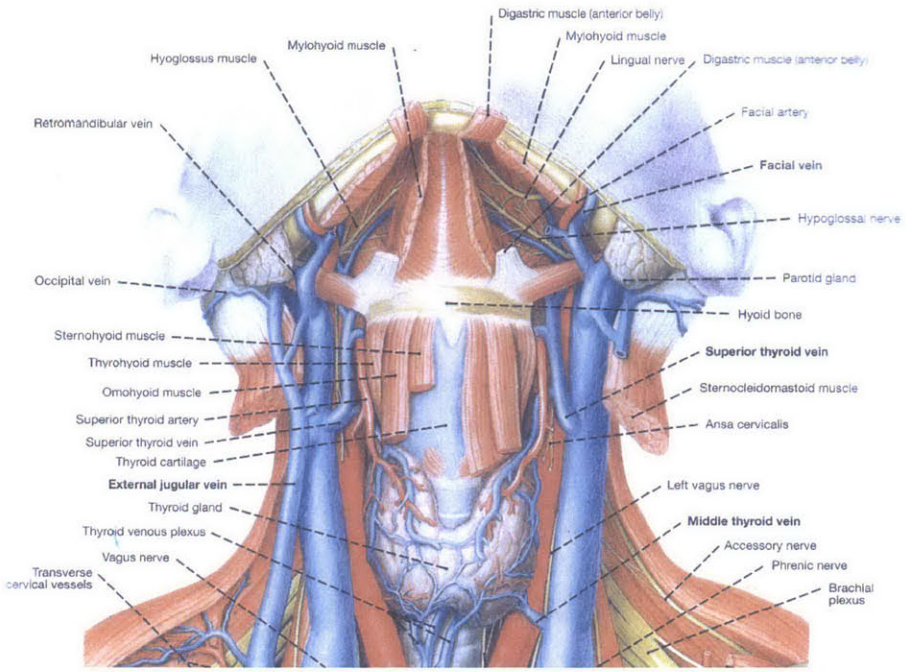

Figure 3-6: Illustration of vascular structures in the neck from [29]

control its own diameter, thereby controlling its vascular impedance. Usually, the reflection at the arterioles overwhelms the reflection at the vascular branchings because the vascular branchings are relatively well matched [27].

A potential arterial site for measuring the ABP waveform is the CCA because it is superficial and close to the head, thus qualifying it for studying hemodynamics in the head. Figure 3-6 shows the vascular structure of the neck. Adjacent to the CCA, the internal jugular vein is located almost in parallel with the CCA. The common carotid artery is further bifurcated into internal and external common carotid arteries. Because of this bifurcation, the reflection of pulse pressure wave may occur but not significantly as that at the arterioles. The average diameter of CCA is reported 6.52 mm for men and 6.10 mm for women [30], and its depth is around 20 mm below the skin.

The BA is also a favorable site not only because it is easily accessible but because the sphygmomanometer measurement is performed on the BA. In addition, the BA mostly stays on the same level as the heart such that the variation of hydrostatic

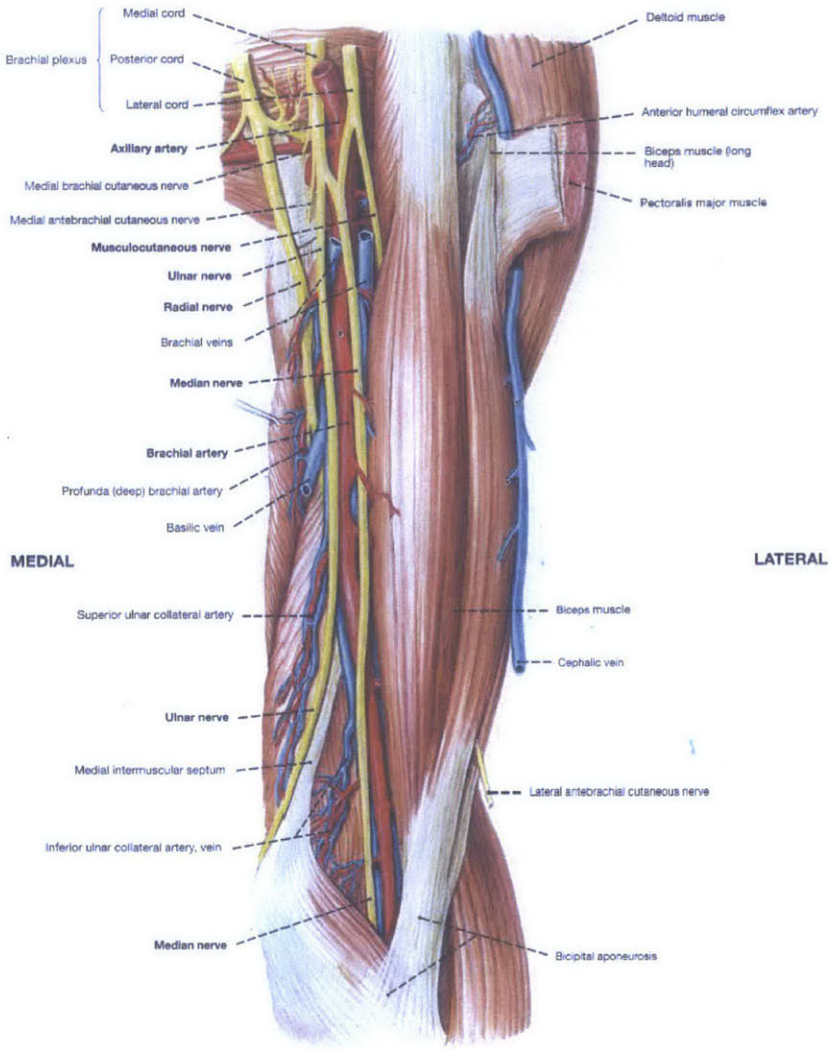

Figure 3-7: Illustration of vascular structures in upper arm from [29]

pressure is insignificant regardless of patients' positions. The BA is eventually divided into the radial and the ulnar artery. Before the division, small minor arteries are branched out as shown in Figure 3-7. The typical diameter of brachial artery is known as 4.4 mm [31].

Chapter 4

Arterial Blood Pressure Waveform Estimation Technique

This chapter first describes an arterial blood pressure (ABP) waveform estimation technique based on hemodynamics of the arterial system described in Chapter 3. In order to estimate the ABP waveform, certain physiological waveforms are required, and they are obtainable using medical ultrasound. This chapter also describes various ultrasonic methodologies to obtain these waveforms and compares their strengths and weaknesses.

4.1 Pulse Wave Velocity

A pulse is the apparent indicator of an arterial vessel dilation in response to a sudden blood pressure increase caused by the rapid contraction of the left ventricle. An arterial vessel dilates to generate sufficient hoop tension to balance against increased blood pressure. In this behavior, the elasticity of a vessel wall determines the amount of a vessel cross-sectional area change given a blood pressure change. In summary, a vessel cross-sectional area is mapped directly to the blood pressure, and the elastic property of the vessel wall quantifies the mapping relationship. Although the mapping is not perfectly one-to-one due to the viscoelastic nature of the vessel wall, this thesis simply models the vessel as a purely elastic tube and focuses on the first order behavior

for simplicity of analysis.

The Bramwell-Hill equation (re-written in Equation 4.1) shows that the PWV (the propagation speed of a pressure wave along an arterial tree) is directly dependent on the compliance of the vessel, thus revealing the elastic property. In fact, the PWV has been widely investigated to indicate cardiovascular diseases due to arterial stiffening. For example, an aortic PWV, reflecting central arterial stiffness, has been indicated as a strong risk factor for cardiovascular diseases [32, 33] and the existence of arteriosclerosis (hardening and narrowing of artery) [34].

The Bramwell-Hill equation (Equation 3.14) is re-written and solved to relate between the pressure (P) and the vessel cross-sectional area (A) as:

$$\begin{aligned} PWV &= \sqrt{\frac{A}{\rho}\frac{dP}{dA}} \\ dP &= \rho PWV^2 \frac{1}{A} dA \\ P(t) - P_{dia} &= \rho PWV^2 \ln(\frac{A(t)}{A_{dia}}) \end{aligned} \tag{4.1}$$

where ρ is the density of blood, A_{dia} is the cross-sectional area at end-diastole, and P_{dia} is the blood pressure at end-diastole. Equation 4.1 quantifies the mapping between the vessel cross-sectional area and the blood pressure with the elastic property of the vessel wall, represented by the PWV. The PWV changes with arterial sites as the area and the compliance vary. Therefore, only a local PWV represents the accurate elasticity which correctly quantifies a pressure-area relationship.

Several techniques have been proposed to estimate the local PWV. A pulse transit time (PTT) method measures the transit time of a distension waveform (the change of a vessel diameter). Then, the local PWV is calculated assuming a distance (D) between two measurement sites is exactly known:

$$PWV_{TT} = \frac{D}{PTT} \tag{4.2}$$

Usually the method tracks a characteristic point in the distension waveform. A foot(onset of systole)-to-foot method has been a standard method because the foot

is relatively insensitive to a waveform distortion caused by the reflection of the pulse pressure wave.

Although the PTT method is straightforward, the accuracy of the method is challenged by errors of a distance measurement and the difficulty of a small transit time measurement, especially in the localized region of interest. Typically, a large transit time over a long distance allows a reliable PWV measurement, which is not available in local PWV estimation. Thus, the PTT method usually requires extremely high temporal resolution (frame rate) to visualize the propagation of the characteristic point in the localized region of view because the PWV is on the order of several m/s. Despite these challenges, several works measured the local PWV using the PTT method [35, 36].

Another method using the temporal and spatial derivative of the distension waveform is presented in [37, 38]. Since the general solution of a wave equation results in the propagating distension wave as $d(\omega t - kx)$, the PWV is calculated as:

$$PWV = -\frac{\partial d(\omega t - kx)}{\partial t} \Big/ \frac{\partial d(\omega t - kx)}{\partial x} = \frac{\omega}{k} \tag{4.3}$$

Finally, the local PWV measurement using a volumetric flow rate (Q) and a cross-sectional area (A) is introduced in [39]. This method, so called QA method, has been studied in ultrasonography [39–41] as well as in MRI [42–44]. Equation 3.14 and 3.19 are combined to result in a PWV expression as:

$$PWV_{QA} = \sqrt{\frac{A}{\rho}\frac{dP}{dA}} = \frac{1}{Z_c}\frac{dP}{dA} = \frac{dQ}{dP}\frac{dP}{dA} = \left.\frac{dQ}{dA}\right|_{reflection-free} \tag{4.4}$$

Therefore, this method estimates the slope of a flow-area plot during a reflection-free period as the local PWV.

The challenge of this method is the synchronized measurement of the flow and the area. Any misalignment of two waveforms results in the distortion of the flow-area plot, thus compromising the local PWV estimate. Another challenge is the limited duration of the reflection-free period during a cardiac cycle, which only appears at the

early systolic stage [39]. In spite of these challenges, the QA method truly estimates the local PWV from a single site measurement.

Although none of the described methods is considered a gold standard, the QA method is further investigated in this work not only because it truly estimates the local PWV at the single measurement site but it provides both the distension and flow waveforms which are two key variables in hemodynamics, thereby allowing to understand the cardiovascular system in a more complete manner.

The QA method requires the flow rate and the area as a function of time. Various ultrasonic methods have been introduced to estimate the blood flow velocity as well as to measure the vessel inner diameter. The following section introduces the theoretical background of these techniques.

4.2 Blood Flow Estimation

A volumetric flow rate refers to fluid volume passing a cross-section per unit time. Its estimation requires not only the flow velocity but the geometrical dimension of the cross-section. This section mainly describes Doppler ultrasound background to measure the velocity of a moving object and various approaches for a flow rate calculation. Cross-sectional area estimation is followed in Section 4.3.

4.2.1 Doppler Ultrasound Theory for a Single Scatterer

Doppler ultrasound has been used for measuring the blood flow velocity based on the Doppler effect. The Doppler effect is defined as a frequency shift between a transmitted and a received wave when a source or an observer moves relatively to each other. The Doppler effect dictates that the frequency shift is proportional to the relative velocity of the object to the observer. In essence, Doppler ultrasound measures the frequency shift of an acoustic wave backscattered from blood to measure the blood flow velocity.

In Doppler ultrasound, there are two ways of operating an ultrasound system. The first one is continuous Doppler ultrasound, which transmits an acoustic wave

continuously, and the spectrum of the transmitted wave is extremely narrow-band. The continuous Doppler ultrasound relies on the actual Doppler effect for its velocity estimate, and the backscattered acoustic wave is observed at a separate ultrasonic transducer because it requires one transducer always transmits the acoustic wave.

Although its operation is straightforward, it is difficult to adjust or re-define a sample volume where the velocity is estimated. The sample volume in continuous Doppler ultrasound is pre-defined by the geometry of a transducer configuration as acoustic beams from the transmit and the receive transducers meet. Because of this limitation, continuous Doppler ultrasound is not widely used in a modern ultrasound system.

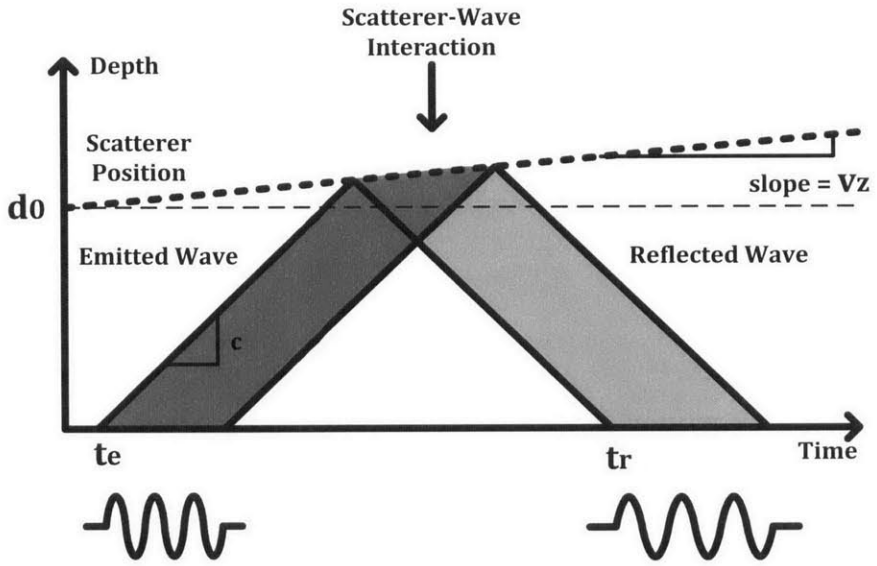

Figure 4-1: Diagram of pulsed Doppler time compression from [15]

The second operation is pulsed Doppler ultrasound, which transmits an acoustic wave in a pulsed way and receive the backscattered echo with the same transducer. One of the great advantages of pulsed Doppler ultrasound is that the sample volume is adjustable in an axial dimension by defining the range gate of the received echo because the round-trip time of the echo contains depth information. The received echo goes through different signal processing compared to continuous Doppler, and its velocity estimate does not rely on the simple Doppler shift. Because of its pulsed

nature, the spectrum of the emitted acoustic wave is wide-band. Although the received acoustic wave certainly has the frequency shift due to the Doppler effect, it is challenging to directly detect this shift like continuous Doppler because of the existence of a frequency dependent attenuation in biological tissues which overwhelms the original Doppler shift. Instead, pulsed Doppler ultrasound estimates the round-trip time shift of the echo as the object moves toward or away from the transducer by comparing consecutively received echoes over time.

A relationship between pulse emitted time (t_e) and pulse reception time (t_r) in Figure 4-1 with a pulse transmission is expressed as:

$$t_e = (\frac{c - v_z}{c + v_z} t_r - \frac{2d_0}{c + v_z}) \approx (1 - \frac{2v_z}{c})(t_r - \frac{2d_0}{c}(1 + \frac{v_z}{c})) \quad (\because \frac{v_z}{c} \ll 1) \tag{4.5}$$

where c is the speed of sound, and v_z is the velocity component perpendicular to a transducer surface [15]. Now, assuming that the emitted acoustic wave is a burst of M cycles of a sinusoid with a frequency of f_0, the emitted pulse ($e(t)$) is given by [14]:

$$e(t) = \prod(\frac{tf_0}{M}) \sin(2\pi f_0 t) \tag{4.6}$$

$$\prod(\frac{t}{T}) = \begin{cases} 1 & 0 \leq t \leq T \\ 0 & \text{otherwise} \end{cases}$$

The received acoustic wave is expressed by using Equation 4.5 and 4.6 as:

$$r(t) = ae(\frac{c - v_z}{c + v_z} t - \frac{2d_0}{c + v_z}) \approx ae((1 - \frac{2v_z}{c})(t - \frac{2d_0}{c}(1 + \frac{v_z}{c}))) \tag{4.7}$$

showing the time compression due to the actual Doppler effect and the time delay due to a round trip. If an acoustic pulse is emitted multiple times, then the emitted acoustic wave is expressed as a train of a sinusoid burst spaced at a pulse repetition time (T_{PRF}) as:

$$e_{mult}(t) = \sum_{n=-\infty}^{\infty} \prod((t - nT_{PRF})\frac{f_0}{M}) \sin(2\pi f_0(t - nT_{PRF})) \tag{4.8}$$

Similarly, the received acoustic wave is expressed in a train of a sinusoid burst with the time compression and the round trip time delay as:

$$r_{mult}(t) = \sum_{n=-\infty}^{\infty} \prod(((1 - \frac{2v_z}{c})(t - \frac{2d_0}{c}(1 + \frac{v_z}{c})) - nT_{PRF})\frac{f_0}{M}) \\ \sin(2\pi f_0((1 - \frac{2v_z}{c})(t - \frac{2d_0}{c}(1 + \frac{v_z}{c}) - nT_{PRF})) \quad (4.9)$$

By sampling at $t = \frac{2(d_0+\Delta d)}{c} + nT_{PRF}$, a sampled signal ($x[n]$) is approximately

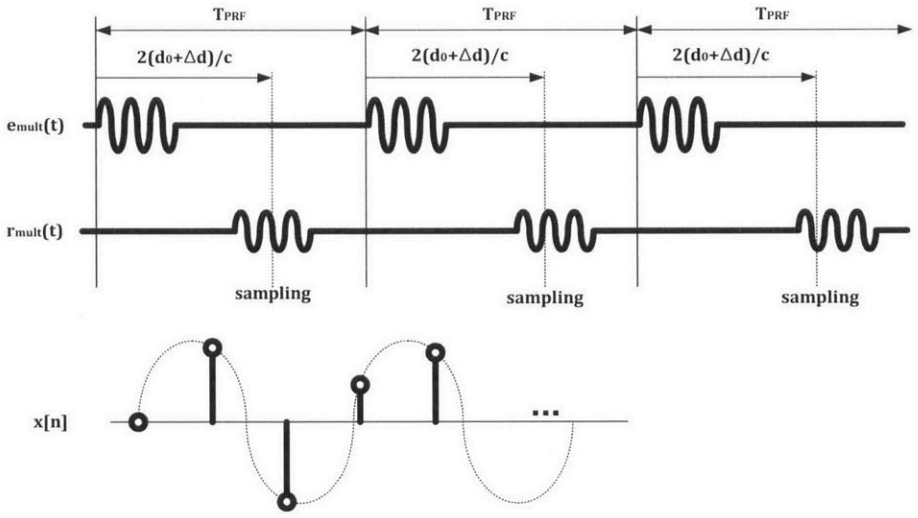

Figure 4-2: Direct sampling for the single range gate of pulsed Doppler ultrasound

expressed as:

$$x[n] = \prod((\frac{2\Delta d}{c} - \frac{2v_z}{c}nT_{PRF})\frac{f_0}{M}) \sin(2\pi f_0(\frac{2\Delta d}{c} - \frac{2v_z T_{PRF}}{c}n)) \quad (4.10)$$

The sampled signal shows a sinusoid with a modulated envelope as the object passes through the sample volume. $x[n]$ has a sampling frequency of a pulse repetition frequency (PRF, f_{PRF}), and the center frequency of $x[n]$ is $f_D = \frac{2v_z f_0}{c}$ in Hz, which is known as a frequency shift in pulsed Doppler ultrasound.

It is noteworthy that the actual Doppler effect also occurs due to the change of a round trip time while the wave interacts with the moving object, thereby changing the frequency (equivalently, the period) of the received wave. Therefore, the round

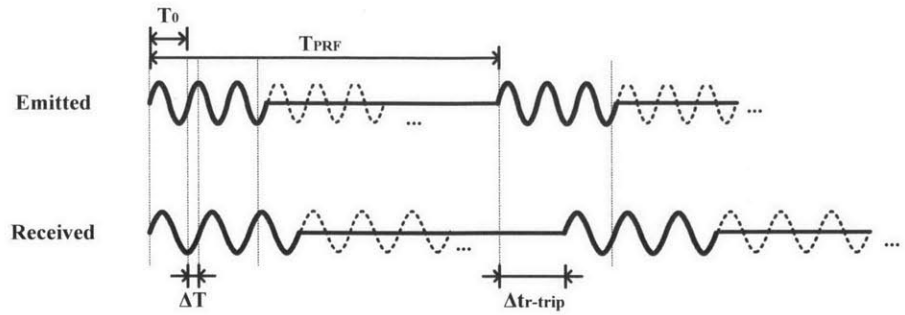

Figure 4-3: Relationship between the round trip time delay in pulsed Doppler and the frequency shift due to the Doppler effect

trip time change between consecutive pulse transmissions can be viewed as the accumulation of the period change (ΔT) of the received wave for T_{PRF} as shown in Figure 4-3 because they all originate from the round trip time change. Converting the round trip time change (Δt_{r-trip}) into the period change (ΔT) of the received pulsed-wave by dividing with the ratio of $\frac{T_{PRF}}{T_0}$, the frequency shift from pulsed Doppler (f_D) becomes the same as the frequency shift (Δf) from the actual Doppler effect, expressed as:

$$\begin{aligned} \Delta T &= \frac{t_{r-trip}}{\frac{T_{PRF}}{T_0}} = \frac{2v_z T_{PRF}}{c} / \frac{T_{PRF}}{T_0} \\ \Delta f = f_0 - (f_0 - \Delta f) &= \frac{1}{T_0} - \frac{1}{T_0 + \Delta T} \simeq \frac{1}{T_0}(\frac{\Delta T}{T_0}) = f_0(\frac{2v_z}{c}) = f_D \end{aligned} \tag{4.11}$$

In essence, the actual Doppler effect estimates the velocity of the object by looking at the round trip time change over a short period of time using the emitted and the received wave. On the other hand, pulsed Doppler estimates the velocity by looking at the round trip time change over a longer period of time using consecutively received waves, which is a different process from the conventional Doppler.

Since Doppler ultrasound measures the velocity component perpendicular to the transducer surface, the actual velocity of the object is expressed as [15]

$$v_{scat} = \frac{c f_D}{2 f_0 \cos(\theta)} \tag{4.12}$$

where θ is an insonation angle. In addition, an aliasing in Doppler spectrum possibly occurs due to the sampling, and the maximum detectable velocity without any ambiguity is dependent on f_{PRF}, f_0 expressed as [15]:

$$v_{scat,max} = \frac{cf_{PRF}}{4f_0 \cos(\theta)} \tag{4.13}$$

It is noteworthy that Equation 4.12 does not show the direction of the moving object. Typically, Equation 4.9 is further processed to a complex signal through either the Hilbert transform or a quadrature sampling followed by the same direct sampling to provide directional information [15].

4.2.2 Volumetric Flow Rate

Assumed Velocity Profile Approach

One of the simplest method to calculate a flow rate is to estimate a complete velocity profile from the maximum velocity assuming the velocity profile is known. In particular, several authors studied this approach in measuring the flow rate through the aortic arch or valve orifices assuming a plug profile [45]. At these sites, blood is subject to high acceleration, and the velocity profile tends to be flat because a viscous drag is insignificant compared to the acceleration from a steep pressure gradient. Another paper uses the Womersley's pulsatile flow model to calculate the flow rate from the maximum velocity measurement [39].

However, the velocity profile is reasonably assumed for the very limited number of cases. As discussed in Section 3.1.2, the velocity profile changes within a single cardiac cycle. In addition, the velocity profile may be asymmetric because of vascular curvatures. Therefore, this approach is generally not well justified in most cases.

Velocity Profile Measurement Approach

To overcome the limitation of the previous approach, the flow rate can be calculated by measuring the complete velocity profile inside the vessel. Figure 4-4 shows

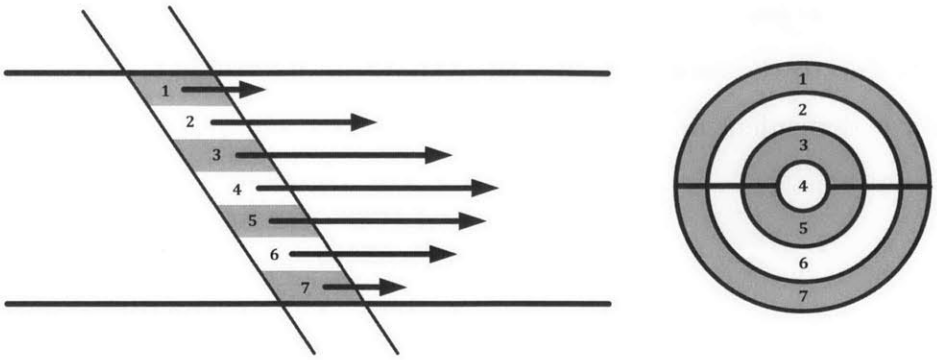

Figure 4-4: Illustrated series of small sample volumes defined along cross-section to measure a complete velocity profile

the diagram of small sample volumes across the vessel lumen. When an acoustic beam insonates through the vessel center, pulsed Doppler ultrasound measures flow velocities from each of the sample volumes. The integration of each velocity over the vessel cross-section with proper weights results in the volumetric flow rate.

This approach requires small sample volumes relative to the vessel dimension so that a velocity gradient within the single sample volume is insignificant otherwise a measured velocity shows a discrepancy from the true velocity profile. Therefore, this approach requires excellent spatial resolution to define the small sample volume. Because of this limitation, it is preferred to measure the flow rate in large blood vessels (10mm in diameter and above) [46].

Uniform Insonation Approach

Uniform insonation is defined as applying an acoustic wave such that an intensity over vessel cross-section is uniform. That is, a beam width is sufficiently large to cover the entire vessel cross-section. The benefit of the uniform insonation is that the received echo is equally weighted over the vessel cross-section. Therefore, a mean frequency shift in a Doppler spectrum is directly related to a spatial mean velocity (an average velocity over cross-section), and the underlying power spectral density represents the number distribution of scatterers (e.g., erythrocytes) moving at the velocity corresponding to the frequency shift. Then, the flow rate is simply calculated

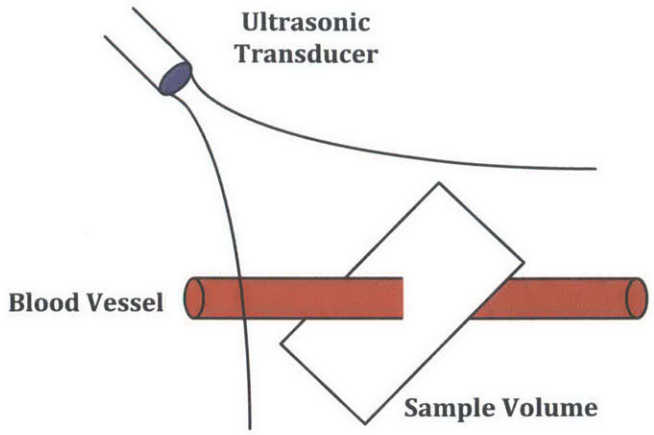

Figure 4-5: Illustration of an uniform insonation approach

as the spatial mean velocity multiplied by the vessel cross-sectional area.

There are mainly three benefits of the uniform insonation approach. First, the uniform insonation does not require high spatial resolution, but the wide beam width is preferred. Second, it is applicable for any velocity profile because the change of velocity profile is always reflected into the underlying power spectral density of the Doppler spectrum. Finally, it is computationally less heavy compared to the velocity profile approach because it requires only one Doppler processing while the velocity profile approach requires several Doppler processings. Several studies have investigated this approach in measuring the volumetric flow rate [47, 48]. In order to achieve sufficient uniformity, the beam width should be sufficiently large compared to the vessel. Because of the finite beam width, the uniform insonation is preferred for flow measurement in smaller blood vessels (less than 10mm in diameter) [46].

The effect of insufficient beamwidth is usually the overestimation of the spatial mean velocity. As seen in Figure 4-6, high velocity scatterers are usually concentrated in the center of the vessel. Knowing that a typical beam pattern is slightly concentrated on the center even with the wide beam width, the high speed scatterers are more pronounced in the Doppler spectrum, thus causing the overestimation. In order to achieve the sufficient beam width, the target vessel should be located at a very far-field region, meaning the natural focus is very close to the transducer. In that

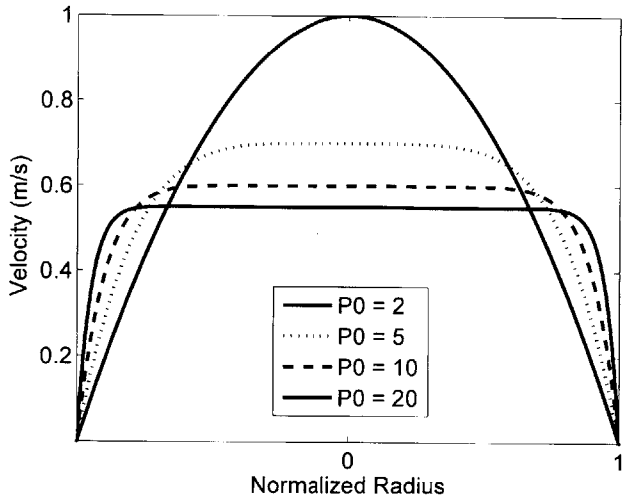

Figure 4-6: Illustration of a velocity profile in different poiseuille profiles

sense, a smaller transducer aperture and a low frequency ultrasound are desirable for the uniform insonation approach. Figure 4-7 shows an overestimation error due to the insufficient beam width.

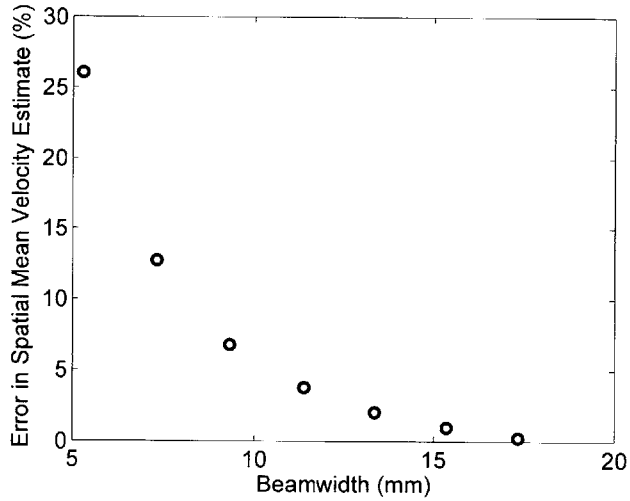

Figure 4-7: Simulation of an overestimated spatial mean velocity in 6.26 mm vessel depending on -3dB beam width

One of the common concerns of Doppler ultrasound in the blood flow measurement is low signal power. As shown in Table 2.2, blood generates weak backscattering. Therefore, the raw Doppler spectrum usually displays a strong stationary echo at DC,

and a weak moving scatterer signal appears next to it. Although a high pass filter rejects the strong stationary echo (clutter rejection), and eventually only the moving scatterer signal is displayed, this relative signal strength also requires an ultrasound system to have a sufficient dynamic range to reliably detect both stationary and moving scatterers. Significantly low signal-to-noise ratio (SNR) due to the weak backscattering leads to the underestimation of the spatial mean velocity because the noise floor of the Doppler spectrum becomes dominant. Figure 4-8 shows a simulated spatial mean velocity underestimation error due to the low SNR. Therefore, the transducer should emit enough acoustic power. Besides, a proper circuit design to achieve a sufficient dynamic range and the SNR is required. Finally, the received signal needs to be conditioned in a digital domain to maximize the SNR in the Doppler spectrum.

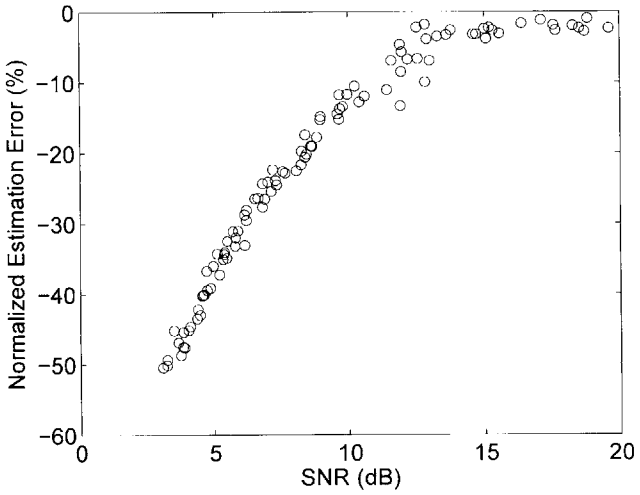

Figure 4-8: Simulation of spatial mean velocity estimate error with the different SNR of a moving scatterer signal in Doppler spectrum

In addition to the previously addressed error sources, the estimate of the spatial mean velocity using the uniform insonation shows a variation as seen in Figure 4-9(a). The backscattered Doppler signal comes from numerous erythrocytes, so the signal is stochastic [15]. Therefore, its mean frequency shift calculated from the Doppler spectrum shows the variation around its true velocity. In a microscopic view, acoustic

waves scattered from red blood cells moving at a different velocity interfere with each other, and a power spectral density at each frequency bin is pronounced or suppressed depending on an interference type (either constructive or destructive) determined by instantaneous scatterer distribution in space.

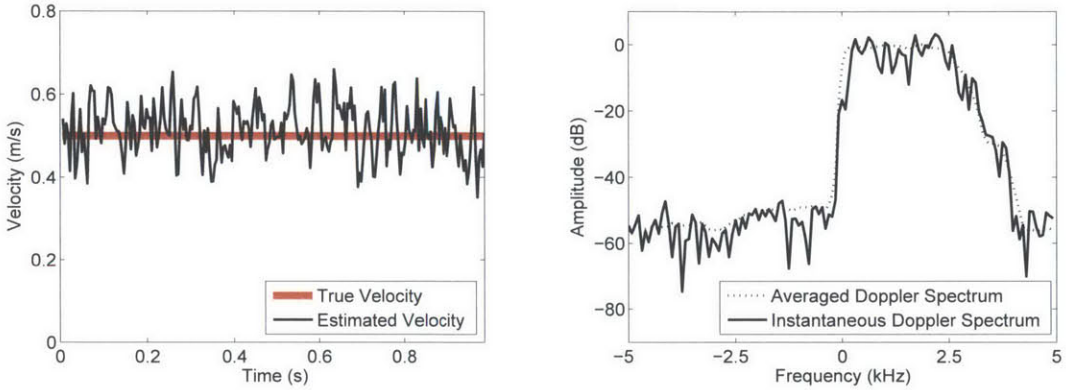

(a) Velocity Estimate

(b) Doppler Spectrum

Figure 4-9: Simulation of a spatial mean velocity estimate variation in a parabolic velocity profile

A low pass filter suppresses the high frequency noise of a flow velocity waveform to reduce the variation. It is reported that 95% of the frequency content of the blood flow velocity waveform at the common carotid artery is concentrated in a frequency band less than 12 Hz [49]. The low pass filter with a cutoff frequency of 20 Hz is utilized in [39, 41].

Another way to suppress the variation is to average multiple flow velocity waveforms obtained in independent sample volumes. Due to the wide beam width in the uniform insonation, spatial mean velocity estimates from thin multiple sample volumes shown in Figure 4-10 approximately follow the same true flow velocity, yet their variation patterns are ideally uncorrelated because each Doppler spectrum originates from different sample volumes. The effect of averaging multiple velocity estimates is clearly visible in Figure 4-11.

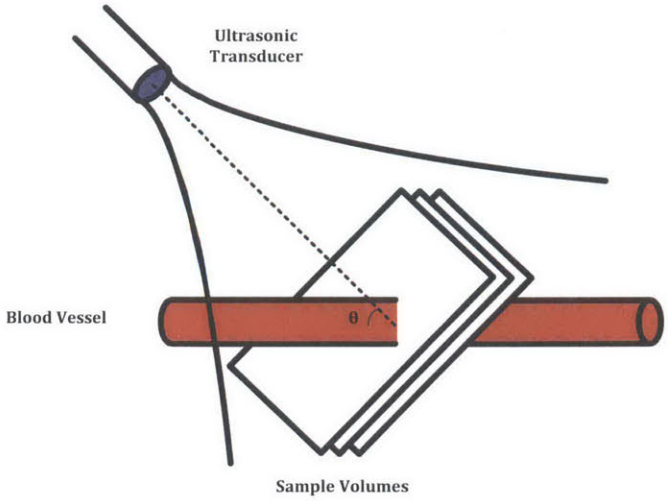

Figure 4-10: Illustration of multiple spatial mean velocity estimates in an uniform insonation

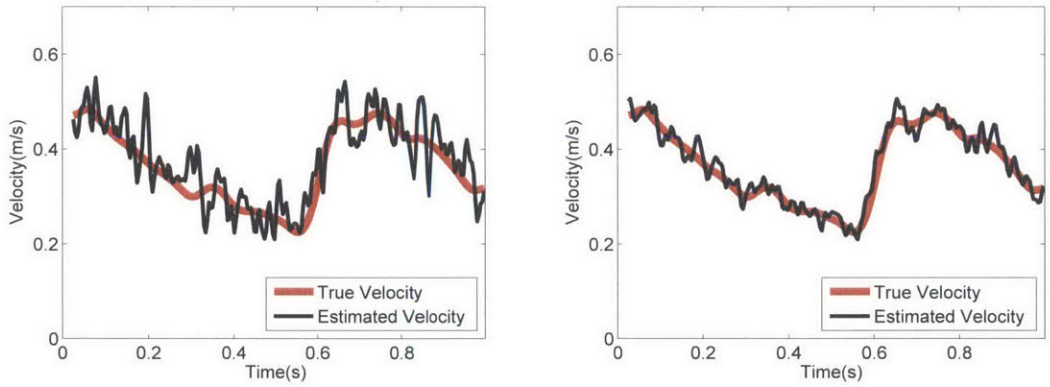

(a) Single Velocity Estimate

(b) Averaged Velocity Estimate

Figure 4-11: Simulation of an averaged spatial mean velocity estimate of seven velocity waveforms from seven sample volumes

4.3 Vessel Cross-Sectional Area Estimation

Although the circular cross-sectional view of a vessel is available in a regular ultrasound scanning, the vessel's inner diameter may be utilized to represent the size of the vessel assuming an axi-symmetric geometry, which is relatively well justified for arteries with sufficient baseline blood pressure. A vessel diameter measurement has clinical importance in detecting plaque, diagnosing arteriosclerosis and determining

a vessel elasticity, and various techniques have been widely investigated. This section concentrates on autonomous vessel diameter measurements.

The cross-sectional area (A) of the vessel is expressed as:

$$A(t) = \frac{\pi d(t)^2}{4} \tag{4.14}$$

where d is the inner diameter of the vessel. For the diameter measurement, ultrasound is transmitted in a pulsed manner to the center of the vessel, and a received signal usually shows distinct echoes coming from wall-to-lumen interfaces. Apparently, the distance between distinct echoes represents the inner diameter. Thus, the identification of two echoes from an anterior and posterior wall is important. In addition, the inner diameter pulsates in response to a blood pressure change, and tracking echo shifts shows the dynamic behavior of a vessel pulsation.

Usually, the received echo contains phase and envelope information. If the wall-lumen interfaces were perfectly identified from the envelope, the complete diameter waveform within a cardiac cycle could be obtained solely from the envelope. Several studies utilized this approach including [50]. However, limited axial resolution and the variation of an echo strength slightly obscure the exact locations of the interfaces. Especially, it is difficult to reliably estimate the tiny echo shift caused by the pulsation between consecutive pulse transmissions purely based on the envelope. Rather, the original echo with both envelope and phase information is considered to be reliable [51] and has been widely studied in various literatures [39, 41, 52]. Therefore, the wall-lumen interface identification from the envelope followed by fine echo shift estimation using the original echo is desirable.

Wall-Lumen Interface Identification

A common technique to locate the wall-lumen interfaces is to find lumen side edges of the echo envelope. A threshold is established to detect a cross-over point where the envelope intersects with the threshold, and the cross-over point is identified as a lumen boundary. The threshold function for reliable boundary detection requires that

the function should depend on the strength of echoes coming from lumen boundaries not only because an absolute echo strength varies in different measurement setups but because multiple strong echoes from different tissue boundaries may exist other than from the lumen boundaries.

The approach so called a sustain attack low-pass filter meets these requirements [53], and it has been utilized to estimate an end diastolic diameter [38,41]. It defines a reference signal ($SA[n]$) decaying as a function of depth, and the reference signal resets to an instantaneous amplitude if it falls below the envelope [38]. This relation is expressed as:

$$SA[n] = \begin{cases} SA[n] = (1 - \frac{c}{2f_s d_{exp}}) \times SA[n-1], & \text{if } SA[n] > Env[n] \\ Env[n], & \text{else} \end{cases} \tag{4.15}$$

where $Env[n]$ is the sampled sequence of the envelope, f_s is the sampling rate of an analog-to-digital converter (ADC), c is the speed of sound, and d_{exp} is the expected diameter of the vessel. Then, the threshold function ($T[n]$) is defined as the fraction of the reference signal as:

$$T[n] = \alpha SA[n] \tag{4.16}$$

where α is the fractional ratio. Similarly, a backward reference signal and a threshold function are defined. Figure 4-12 shows the envelope with the threshold functions. The intersection of the forward threshold at the trailing edge of the last dominant echo before the lumen is denoted as the anterior wall boundary. Similarly the intersection of the backward threshold at the rising edge of the first dominant echo after the lumen is denoted as the posterior wall boundary. However, the exact lumen diameter has to be corrected for the axial resolution of an ultrasound system because the anterior boundary is detected at the trailing edge of the received echo [54].

Echo Tracking

Echo tracking refers to various techniques which estimate the fine movement of

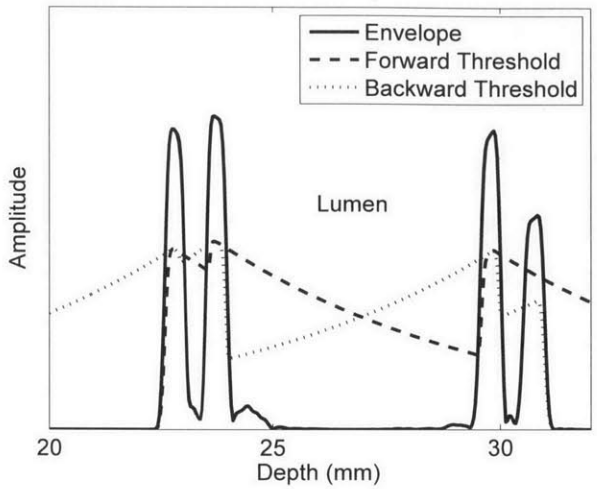

Figure 4-12: Simulated echo with a threshold function set by sustain attack filter approach

the echoes from the lumen boundaries over a cardiac cycle. The echoes that are to be tracked are determined from the identified lumen boundaries. Typically, this technique estimates an anterior wall velocity (v_{ant}) and a posterior wall velocity (v_{pos}) based on a short data segment windowing the echoes from the boundaries, thus greatly relieving a data rate requirement. By comparing two consecutive received signals, the wall velocities are estimated. Subsequently, the integration of an anterior and posterior wall velocity difference results in a diameter change (Δd), expressed as:

$$\Delta d(t) = d(t) - d(0) = \int_0^t (v_{pos} - v_{ant})dt \tag{4.17}$$

The estimated diameter change is robust to a transducer motion because the motion is canceled out in the subtraction of wall velocities. However, any biased velocity estimate causes an accumulated error, thus causing the baseline drift of the diameter waveform.

The wall velocity in a radial direction is very low (several mm/s) compared to the blood flow velocity, and the echo shift between consecutive pulse transmissions is so small that conceptually an echo shift estimator needs to interpolate the sampled echo (with the ADC) to achieve finer velocity estimate resolution. Several echo shift

estimators have been introduced based on the sinusoidal nature of the received echo signal. For example, a shift estimator based on correlation interpolation for a band-limited signal is presented in [55], and the autocorrelation ($R_{SS}(U)$) of a moving echo signal ($S(U)$) is given by

$$R_{SS}(\Delta X, \Delta T) = R_{SS}(\Delta U) = \frac{\omega_b}{\pi} S_0 \cos(\omega_c \Delta U) \frac{\sin(\omega_b \Delta U/2)}{\omega_b \Delta U/2} \tag{4.18}$$

where $U = X - vT$, S_0 is the power spectral density, ω_c is the center frequency, ω_b is the bandwidth of $S(U)$, and v is the velocity of the moving echo. For a narrowbanded echo ($\omega_b \ll \omega_c$), Equation 4.18 is simplified to have only cosine dependency, and the peak of R_{SS} ($\Delta U \ll 1$) is further approximated into a parabola.

From the sampled received echo sequence, a parabolic approximation allows to estimate the fine echo shift using only three points around the peak of the cross-correlation of two consecutive echoes ($\Delta T = T_{PRF}$). The interpolated peak position of the cross-correlation function ($\hat{R}_{12}$) is expressed as [15]:

$$n_{peak} = n_m - \frac{\hat{R}_{12d}[n_m + 1] - \hat{R}_{12d}[n_m - 1]}{2(\hat{R}_{12d}[n_m + 1] - 2\hat{R}_{12d}[n_m] + \hat{R}_{12d}[n_m - 1])} \tag{4.19}$$

where n_m is the peak of $\hat{R}_{12}$. Then, the estimated echo velocity is given by

$$\hat{v}_{peak} = \frac{c}{2} \frac{n_{peak} f_{PRF}}{f_s} \tag{4.20}$$

where c is the speed of sound, f_{PRF} is the pulse repetition frequency, and f_s is the sampling frequency of the ADC.

Although this approach is simple, the bandwidth of the echo is usually wide due to a pulsed operation. The Cross-Correlation Model (CCM) estimator models the spectral content of the received echo as Gaussian shape [56]. The benefit of this estimator is that it does not assume the bandwidth of the echo. Subsequently, The Complex Cross-Correlation Model (C3M) estimator uses a complex analytic echo signal obtained from either the Hilbert transform or a quadrature sampling [57]. It is shown that the C3M estimator shows less bias error than the CCM estimator. The

velocity estimate of the C3M estimator is given by:

$$\hat{v} = \frac{c}{2}\frac{f_{prf}}{f_s}\frac{\arg(\hat{R}[0,1])}{\arg(\hat{R}[1,0])} \tag{4.21}$$

where $\hat{R}$ is the cross-correlation of two analytic echo signals. $\hat{R}[0,1]$ represents a zero-lag cross-correlation between two complex echo signals between consecutive pulse transmissions.

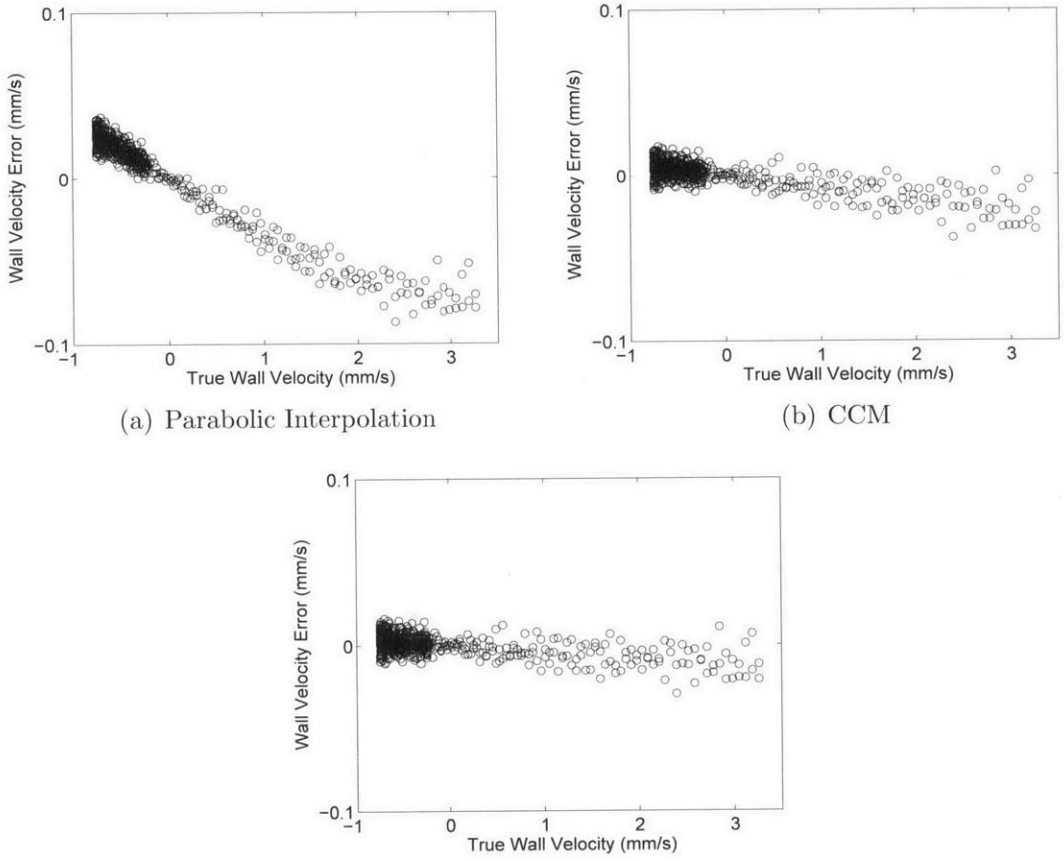

(a) Parabolic Interpolation

(b) CCM

(c) C3M

Figure 4-13: Simulated performance comparison of echo shift estimators for vessel wall velocity estimation

Figure 4-13 compares the performance of the introduced echo shift estimators. The parabolic interpolation shows significant bias error. On the other hand, the CCM and the C3M estimator show less bias error. The C3M estimator shows a superior result to the CCM estimator, which is expected by [57]. Figure 4-14 shows

simulated diameter change estimation using the C3M estimator over sixteen cardiac cycles. Assuming an end-diastole diameter is properly measured at the beginning, the C3M estimator shows a superior echo tracking performance, resulting in an accurate diameter change estimate. However, since no estimator is completely free of bias error, it is desirable to periodically re-identify lumen boundaries to reset any possible baseline drift in the diameter waveform.

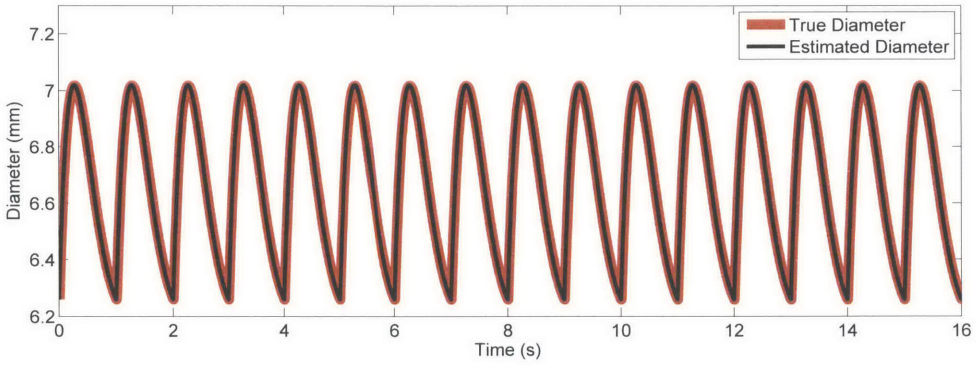

Figure 4-14: Simulation of an estimated diameter change over sixteen cardiac cycles using the C3M estimator

Chapter 5

Experimental Test

5.1 Experimental Setup

An experimental test conducted in a well-controlled environment is desirable to clearly understand the limitations and possible error sources of the proposed technique. A custom designed experimental setup (shown in Figure 5-1) was built to test the pressure estimation technique. The experimental setup consists of three parts: a flow phantom, a custom-designed ultrasound system with supporting electronics and a pressure sensor setup to measure a reference pressure waveform.

5.1.1 Flow Phantom Characterization

The flow phantom consists of a tank filled with water, a latex rubber tube, a graduated cylinder and a diaphragm pump. Water acts as the medium of an acoustic wave and mimics tissue with negligible attenuation. The pump is operated by DC voltage, and it provides enough pressure to generate a flow rate similar to that of major arteries with a given flow circuit. In addition, it also mimics the pulsatile nature of the heart by supply voltage modulation, and responds to the voltage change fast enough to generate pulsatile pressure and flow. Since the water pump draws a significant amount of current, a switching regulator is used to reduce power dissipation. This switching regulator performs DC to DC conversion, but its output voltage is controlled

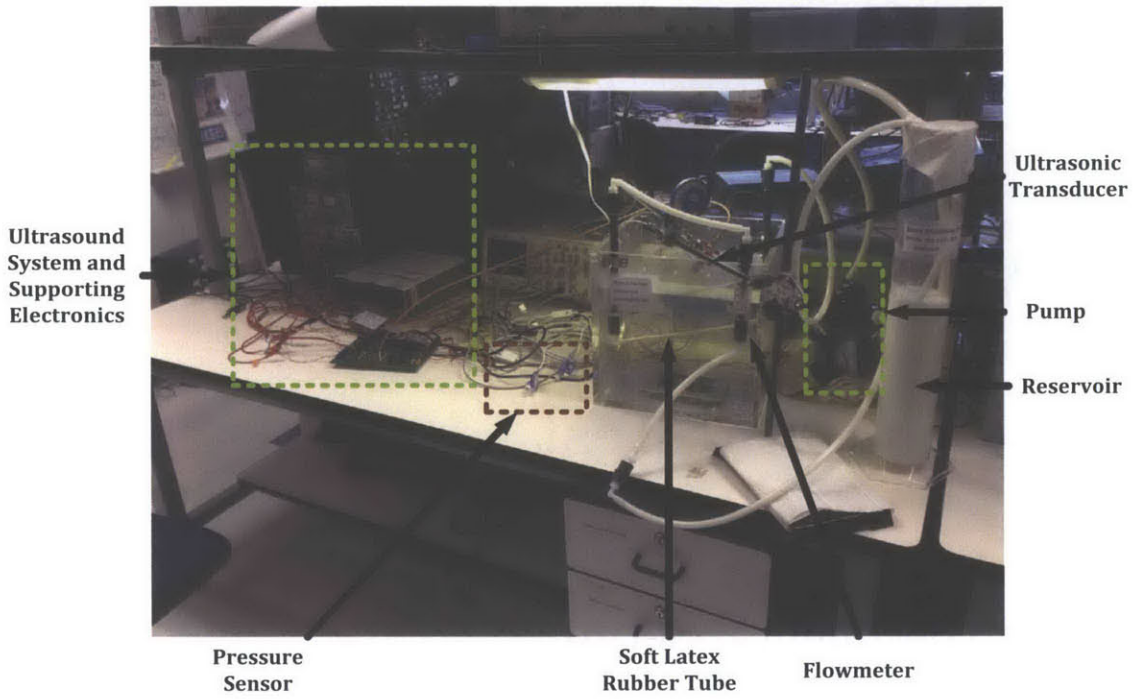

Figure 5-1: Experimental setup

by a reference signal fed by a signal generator. Hence, the signal generator virtually controls the pump, which allows easy manipulation of the supply voltage of the pump.

A key discrepancy between the pump and the heart is that the pump generates various pressures and flow rates by changing the frequency of its diaphragm motion instead of a huge pumping motion. Figure 5-2 compares two spectra of measured pressure waveforms with different pump voltages (V_{supply}). As the supply voltage increases, the frequency of the secondary peak increases, indicating the more rapid diaphragm motion. In this flow phantom, therefore, finite duration pressure impulses from each diaphragm motion superpose to generate output pressure which is further smoothed by the flow phantom. Undoubtedly, the pump still generates a reasonable pulsatile pressure waveform. However, possible limitation due to this mechanism is that although the supply voltage of the pump is periodically controlled, the onset of a resulting pressure waveform may vary slightly depending on the phase in its diaphragm motion. As a result, the generated pressure waveform may not be completely periodic even though the supply voltage is periodic.

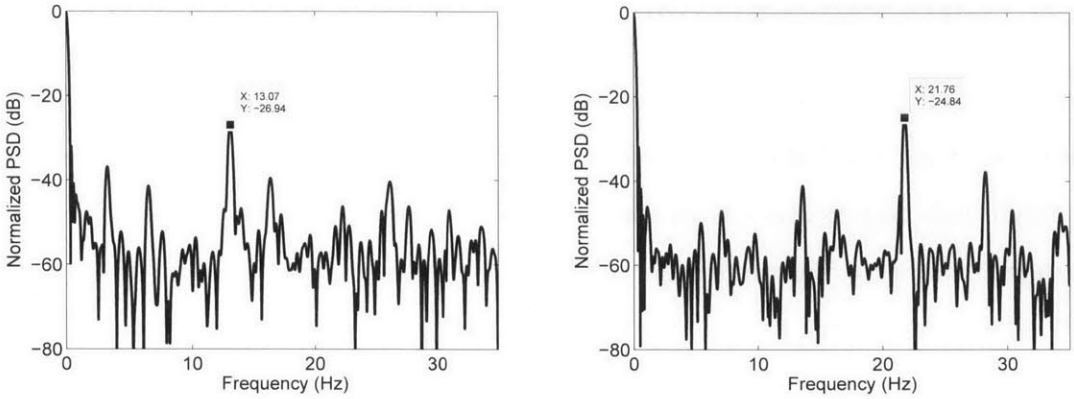

(a) V_{supply}= 2.23 VDC (b) V_{supply}= 3.24 VDC

Figure 5-2: Measured power spectral density of pressure waveform in constant pump supply voltage

The flow phantom starts from the pump and proceeds to a flowmeter, a rigid tube and a connection to a soft latex rubber tube. The latex rubber tube mimics an arterial vessel segment, and its material meets A-A-52047C standard. This commercial item description does not specify an exact Young's modulus, but based on the tensile stress at 100% elongation, this tube may reasonably mimic an arterial vessel segment. The latex rubber tube segment is 30 cm long, and it runs along the diagonal of a horizontal plane to maximize the segment length. After the latex rubber tube, the phantom goes to a reservoir (graduated cylinder) where air bubbles are captured at fluid surface for debubbling the phantom.

The flow phantom circulates blood mimicking fluid (Shelley Medical Imaging Technologies, London, Ontario, Canada). The blood mimicking fluid (BMF) consists of 5-μm diameter nylon particles acting as ultrasonic scatterers, and these particles are suspended in the fluid base of water, glycerol, dextran and surfactant to maintain an uniform distribution and to match the physical and acoustic properties of blood [58]. The BMF provides realistic acoustic scattering closer to *in vivo* situation.

5.1.2 Ultrasound System

Two single element transducers are positioned to insonate the tube at 90 degrees and 50 degrees. Figure 5-3 shows a typical transducer setup. The ultrasonic transducer of channel one measures a spatial mean velocity through pulsed Doppler ultrasound. In order to uniformly insonate the tube, the operating frequency and the aperture size (2 MHz and 6 mm) are selected to maximize the uniformity of the beam pattern. In addition, the transducer is positioned at 130 mm away from the vessel center. However, because of the long round-trip time of an acoustic wave, a pulse repetition frequency (f_{PRF}) is limited to 5 kHz which sets the upper limit of a maximum detectable velocity avoiding any aliasing in Doppler spectrograms. In this configuration, the maximum detectable velocity is 1.50 m/s which is sufficient considering that the maximum blood flow velocity of the common carotid artery is about 1.2 m/s [49].

The ultrasonic transducer of channel two insonates the tube perpendicularly to maximize the strength of echoes from wall-lumen interfaces for diameter estimation. Strong echoes from the wall-lumen interfaces are detected to accurately estimate a

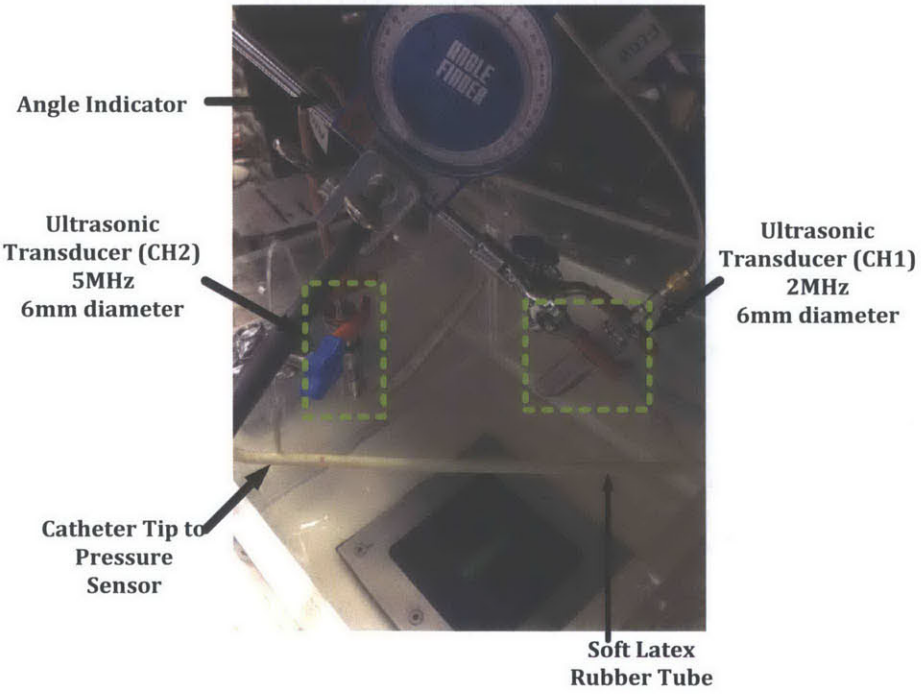

Figure 5-3: Two ultrasonic transducers configuration

vessel diameter. Although the depth of the latex rubber tube ($\sim$ 85 mm) is not realistic for superficial arteries, the more realistic realization of this approach is available using a different transducer design possibly from custom manufacturers. This experiment, instead, focuses on the proof of concept of the pressure estimation technique with the simple configuration of two single element transducers.

A custom-designed ultrasound system is utilized for driving two ultrasonic transducers, receiving and processing echo signals. Although the system is designed for other application, it is still usable for this experiment. The power of the ultrasound system is supplied from a single 5.5V DC power supply and a +25V and -25V high voltage supply rail. A power management circuitry provides different supply voltages to individual blocks. A high voltage pulser directly drives the ultrasonic transducers. The processed data is streamed to a laptop using a UART (Universal Asynchronous Receiver Transmitter)/USB (Universal Serial Bus) bridge. The transmitted bit stream is captured and further post-processed using MATLAB (MathWorks, Natick, MA). Details of the ultrasound system are referred to [59].

5.1.3 Pressure Sensor

In order to compare a pressure waveform obtained from ultrasonic methods, a reference pressure waveform is directly measured using a pressure sensor (Utah Medical Products Inc., UT, USA). The flow circuit is accessed at the proximal and distal sites of the latex rubber tube segment through catheter tips, and the tips are individually connected to two pressure sensors through rigid tubings. The pressure sensor correctly measures the pressure in the tube while no pressure drop occurs due to flow in the rigid tubing. The pressure sensor then converts pressure into a differential voltage signal. The differential voltage signal is amplified with a gain of 100 through an instrumentation amplifier with a single-ended output. This signal is then measured by an oscilloscope.

5.2 Experimental Procedure

This section describes an overall signal processing flow in the ultrasound system and also a typical experimental procedure to obtain experimental results.

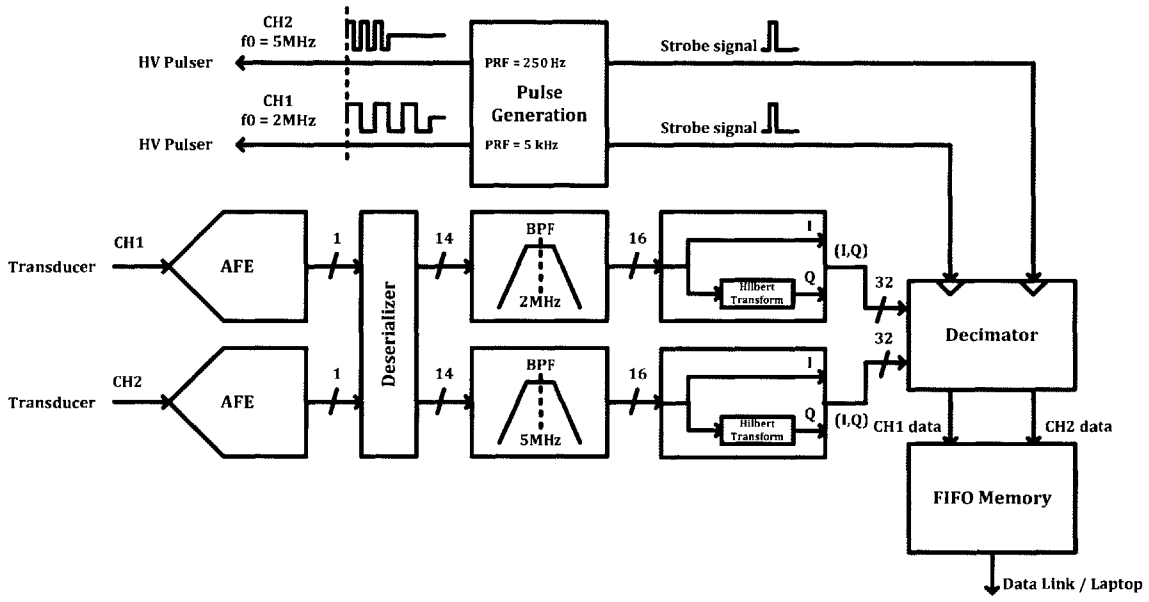

Figure 5-4: Two channel signal processing block diagram

Two separate channels are utilized for driving the transducers, processing raw signals and converting into meaningful data. Figure 5-4 shows an overall block diagram of the signal processing in an analog domain and a digital domain. The ultrasound system transmits a burst of square waves with a specified pulse repetition frequency (PRF) to the high voltage (HV) pulser which directly drives the transducers. A strobe signal generated at each pulse transmission provides a time of reference for a decimator to chop data within the region of interest. A received voltage signal is amplified through a low noise amplifier (LNA) and a digitally controlled variable gain amplifier (VGA) with an attenuator. Different gain settings are applied for each channel to maximize signal quality. Then, the amplified voltage signal is digitized through an analog-to-digital converter (ADC), and a series bit stream is transmitted to a field programmable gate array (FPGA). The FPGA deserializes the incoming bit stream, and the deserialized data is bandpass filtered to maximize the signal-to-noise ratio

(SNR) and suppress any noise from a power line. The main lobe width of a bandpass filter is roughly matched to that of the transmitted pulser voltage waveform. The resulting signal is converted to an analytic signal by the Hilbert transform, and the decimator selects necessary data points.

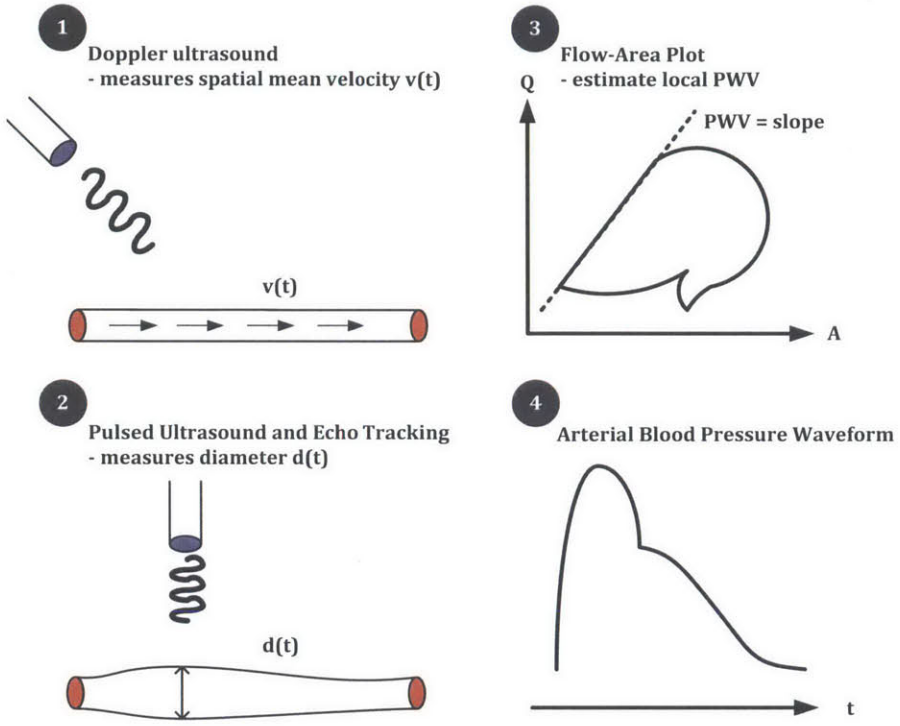

Figure 5-5: Illustration of signal processing flow from raw physiological waveforms to pressure waveform

A typical experimental procedure starts from measuring the minimum absolute diameter of the latex rubber tube using the sustain-attack filter approach. Since the flow phantom is not completely periodic, the minimum diameter is measured multiple times to calculate an average minimum diameter, and echoes from anterior and posterior wall-lumen boundaries are properly identified. Then, the ultrasound system operates both channels to measure a spatial mean velocity and a diameter change for sixteen seconds, limited by maximum data rate and a memory size. A flow-area plot is drawn by combining the spatial mean velocity and the diameter to calculate a local pulse wave velocity (PWV) estimate. Finally, a pressure waveform estimated by ultrasonic methods is directly compared with the reference waveform

from the pressure sensor. Figure 5-5 shows a high level waveform processing flow.

5.3 Experimental Results

This section provides experimental results to test the validity of the pressure waveform estimation technique for continuous and non-invasive blood pressure monitoring. First, the pressure sensor is characterized to provide the correct reference pressure waveform. Second, the spatial mean velocity using the uniform insonation is verified with a flow phantom with micro-bubbles used as scatterers. Then, the QA method to estimate the local PWV is experimentally verified. Finally, this section concludes with pressure waveform comparison.

5.3.1 Pressure Sensor Calibration

In order to obtain the reference waveform, pressure sensors (Utah Medical Products Inc., UT, USA) are connected to the proximal and the distal site of the latex rubber tube segment. A resulting differential voltage signal is proportional to an applied pressure and an excitation voltage which is supplied from an external voltage source. The proportionality is defined as a sensitivity, and it is written as:

$$V_{out} = \text{Sensitivity } (\mu V/V/mmHg) \times \text{Pressure } (mmHg) \times V_{excitation}(V) \qquad (5.1)$$

Even with the excitation voltage rated by the manufacturer, an expected differential output voltage is only few milivolts, thus requiring amplification to be read by an oscilloscope. The instrumentation amplifier amplifies the original differential signal by a gain of 100. In order to measure the sensitivity, a pressure gauge, which provides an accurate pressure measurement in a constant pressure setup, is installed at downstream after the latex rubber tube.

The resulting voltage signal (amplified by 100) and the pressure reading from the pressure gauge are plotted in Figure 5-6 to calculate the sensitivity of the pressure sensor. The plot clearly shows the linear relationship between the resulting voltage

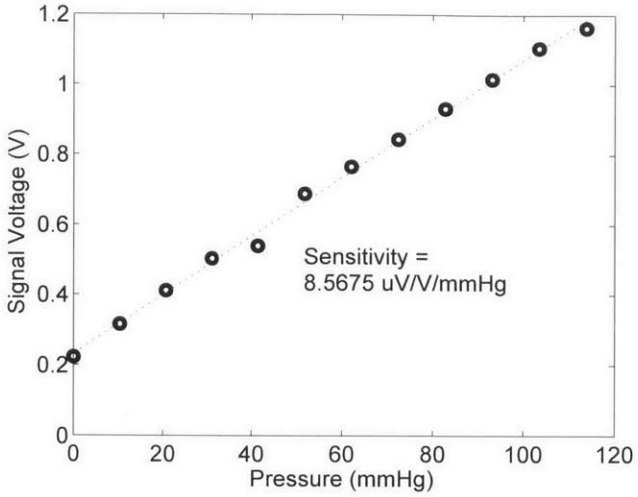

Figure 5-6: Measured sensitivity of a pressure sensor

and the pressure reading. Given that the excitation voltage is 9.8V, the sensitivity is 8.57 uV/V/mmHg.

There are potentially two major sources of error in Figure 5-6. The first one is an offset error which is introduced by the hydrostatic pressure of fluid column between the catheter tip and the pressure gauge site. In this experiment, the pressure gauge site is located 25 cm above the catheter tip, implying the pressure at the latex rubber tube is about 20 mmHg higher than the pressure gauge site. This offset error translates all data points rightward, but it essentially does not affect the sensitivity measurement itself.

The other error is a flow rate dependent pressure drop from the catheter tip to the pressure gauge site due to a viscous resistance. Given that the diameter is 6.26 mm and the distance between two sites is 25 cm, an expected pressure drop at the flow rate of 31.5 cm^3/s (about an average flow rate in this experiment) is only 1.57 mmHg. Therefore, Figure 5-6 contains a gain error although it is considered negligible.

5.3.2 Flow Velocity Measurement

A spatial mean velocity measurement using the uniform insonation is tested in the flow phantom. The flowmeter is installed into the flow phantom to provide a reference

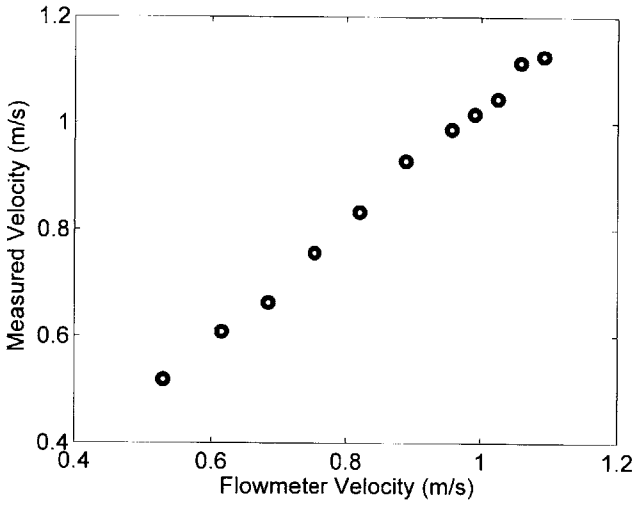

Figure 5-7: Spatial mean velocity measurement using an uniform insonation

flow velocity measurement. Since the flowmeter is manufactured to measure a water flow rate, the flow phantom circulates water, and microbubbles act as scatterers. The rigid tube with a diameter of 6.26 mm, measured with a caliper, replaces the latex rubber tube to keep a constant inner diameter.

Figure 5-7 shows an estimated spatial mean flow velocity. The estimated velocity slightly overestimates in a high flow rate region, but generally the result matches the flowmeter velocity. In order to represent the accuracy, a normalized root mean square error (NRMSE) is defined as following:

$$NRMSE = \frac{1}{x_{max,est} - x_{min,est}} \sqrt{\frac{1}{N} \sum_{i=1}^{N} (x_{est,i} - x_{obs,i})^2} \tag{5.2}$$

where x_{est} is the estimated flow velocity using the uniform insonation, x_{obs} is the observed flow velocity using the flowmeter, and N is the number of data points. The calculated NRMSE is 2.84%, which demonstrates the high accuracy of this measurement and a good agreement with experimental results from the previous work [59].

5.3.3 Pulse Wave Velocity Measurement

This section describes the experimental result of the local PWV estimation using the QA method. In this experiment, blood mimicking fluid (Shelley Medical Imaging Technologies, London, Ontario, Canada) emulates blood's mechanical properties and Rayleigh scattering from erythrocytes. The flow phantom is debubbled as much as possible by collecting air bubbles spontaneously at the fluid surface in the reservoir while circulating the blood mimicking fluid for a long time. This debubbling ensures to minimize artifacts from microbubbles.

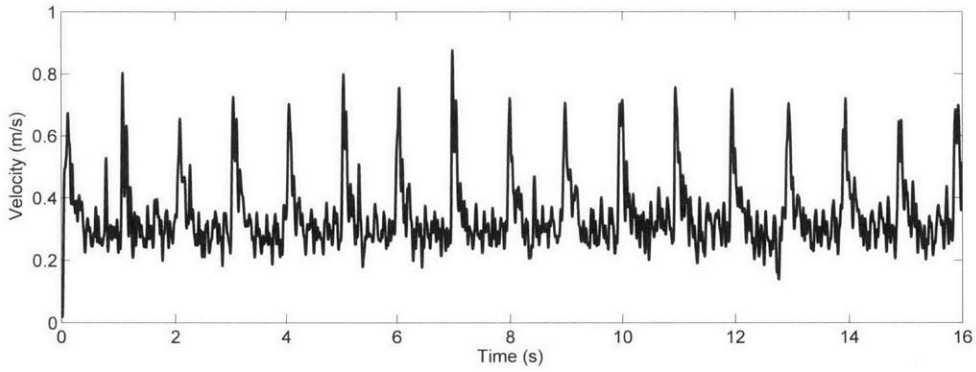

Figure 5-8: Measured spatial mean flow velocity in periodic pulsatile flow

Figure 5-8 shows a typical spatial mean velocity waveform in the pulsatile flow with a nominal period of one second. The waveform has a sampling rate of 250 Hz. It shows the steep increase of the flow velocity every second, which mimics the onset of the systolic phase at every cardiac cycle. The flow rate is determined to roughly match a volumetric flow rate in the common carotid artery while minimizing microbubble generation. It is important to minimize microbubbles because strong backscattered echoes from any microbubbles dominate a normal moving scatterer signal, thus resulting in the flow velocity of microbubble instead of the true spatial mean velocity. At the beginning, the waveform shows a transient response from a clutter rejection filter, which can be discarded during a real-time operation.

A complete diameter waveform consists of the pulsatile change of the diameter on top of an absolute diameter measurement. Figure 5-9 shows an envelope of a received

echo overlaid with a forward and a backward threshold using the sustain-attack filter approach [53]. The intersections of the thresholds and the envelope are identified as wall-lumen boundaries. Four distinct echoes, although the last echo is not apparently distinct, represents four boundaries: water to anterior wall, anterior wall to lumen, lumen to posterior wall and posterior wall to water. An average minimum diameter of the data set presented in Figure 5-9 is 6.22 mm. The diameter measurement is corrected with the axial resolution of the ultrasound system because the anterior lumen boundary is identified with the trailing edge of the echo (denoted A in Figure 5-9).

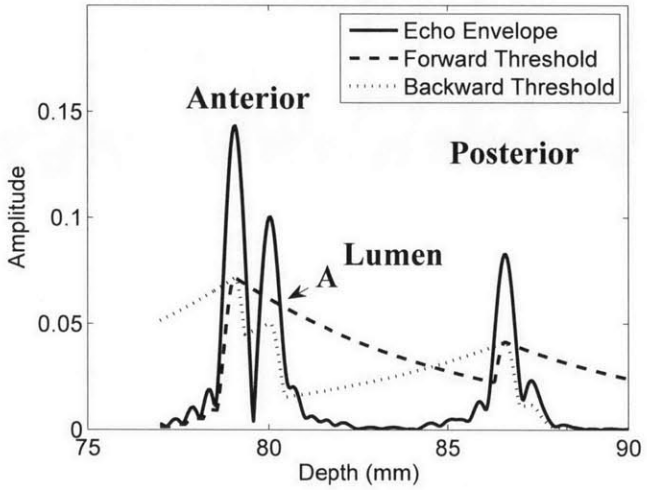

Figure 5-9: Wall-lumen interface identification using sustain-attack filter approach from the envelop of a measured echo

Figure 5-10 shows the typical diameter waveform with a sampling rate of 250 Hz. The pulsatile change of diameter is estimated by tracking the echo at the identified wall-lumen interfaces from Figure 5-9 using the C3M estimator [57]. The diameter also drastically increases at the onset of the systolic phase which reflects the drastic increase of the internal pressure. The flow velocity waveform from Figure 5-8 and the diameter waveform from Figure 5-10 are obtained simultaneously in order to avoid any synchronization issues.

The spatial mean velocity and the diameter waveform are low-pass filtered with

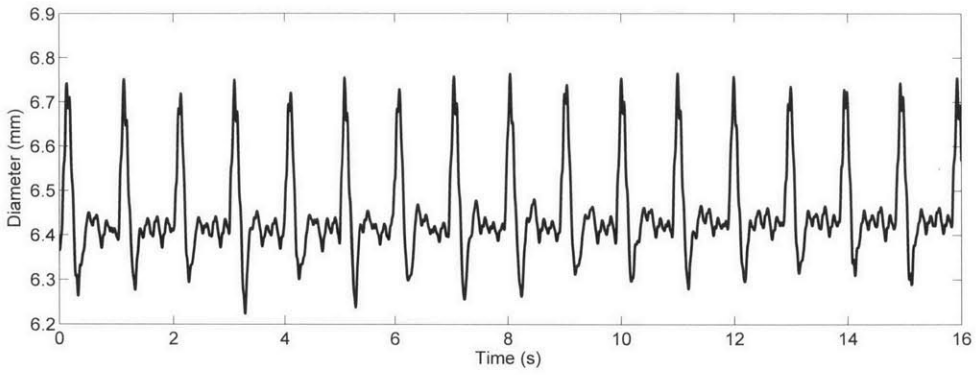

Figure 5-10: Measured pulsatile diameter waveform in periodic pulsatile flow

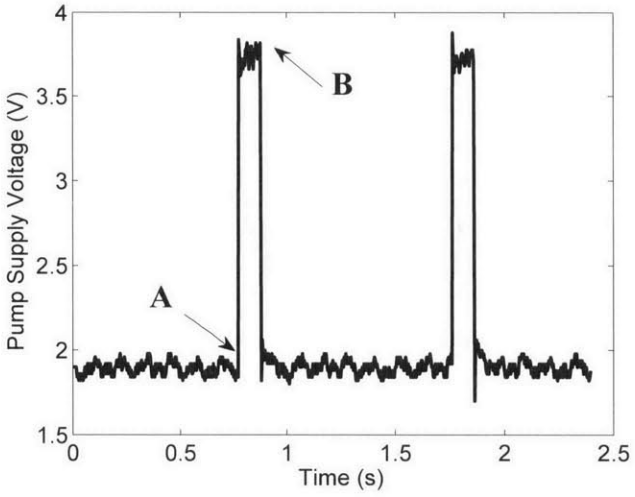

Figure 5-11: Measurement of the typical supply voltage waveform of the pump

a cutoff frequency of 30 Hz and averaged over multiple cardiac cycles to result in smoother waveforms. Then, a volumetric flow rate and a cross-sectional area are calculated and plotted in a flow-area plot as shown in Figure 5-12.

At the beginning of a simulated cardiac cycle (denoted A in Figure 5-11), the pressure, equivalently represented by the area, and the flow rate increase simultaneously for about 50 ms. However, a pulse pressure wave and a flow wave are propagated along the latex rubber tube and reflected where the latex tube and the rigid connector meet. Then, the reflected wave whose flow component is sign-reversed returns to an observation site which is located at the proximal site of the rubber tube segment.

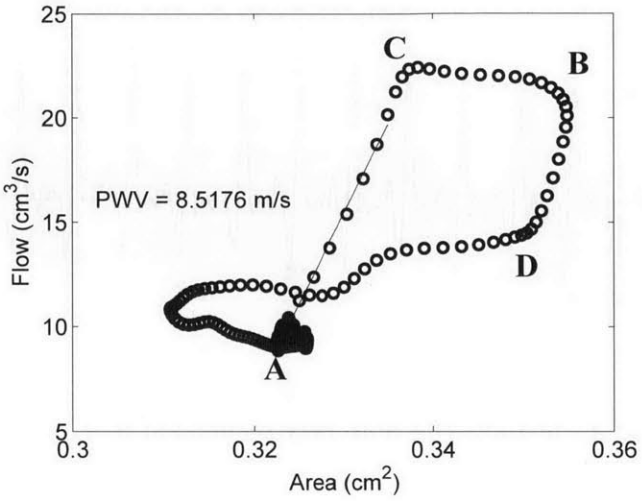

Figure 5-12: Measurement of a typical flow-area plot

As a result, the reflection hinders a flow increase while the area increases further. In Figure 5-12, the clockwise rotation of a flow-area loop (denoted C) represents the effect of the reflected wave. Then the flow and the area decrease simultaneously at the end of the systolic phase in the cardiac cycle (denoted B in Figure 5-11 and 5-12). Once again, the effect of reflection rotates the flow-area loop in a clockwise manner (denoted D in Figure 5-12). Then, the flow-area loop gradually returns to its resting point.

The flow-area plot clearly shows a linear phase at the beginning of the systolic phase which is predicted during a reflection-free period. According to the QA method, the slope of this linear phase estimates the local PWV, and the estimated local PWV of this data set is 8.52 m/s. Considering a round trip distance from the observation site to the reflection site is about 50 cm, an expected round trip time with the estimated PWV is approximately 58 ms, which roughly agrees with the duration of the reflection-free period (50 ms) in Figure 5-12.

Figure 5-13 shows the comparison of the pressure waveform from ultrasonic methods and the reference waveform from the pressure sensor assuming an average pressure over a single cardiac cycle is the same, thus comparing only a pulsatile component. Two waveforms agree to each other with minor discrepancies. These discrepancies

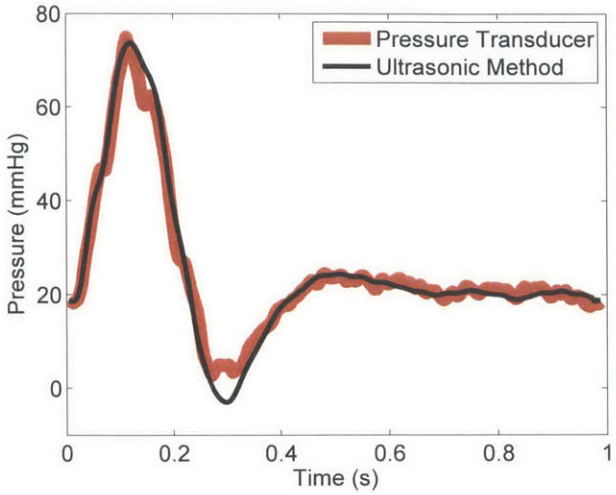

Figure 5-13: Comparison of averaged pressure waveforms from 1) ultrasonic methods and 2) pressure sensor measurement

are mainly attributed to the difference in the number of cardiac cycles for averaging waveforms and, most importantly, to the non-simultaneous measurement of two waveforms because the flow phantom is not completely periodic. Finally, the discrepancy in a low-pressure region where the ultrasonic method underestimates the pressure seems to originate from the non-symmetric contracting of the rubber tube. This phenomenon becomes less apparent as the low pressure region gets elevated.

The accuracy of the local PWV estimate is tested in direct comparison of two pressure waveforms. Since the PWV is closely related to the compliance of the tube (area increment per unit pressure increase), a scaling error is a good metric to test the accuracy of the local PWV estimate, and it is defined as:

$$\text{Scaling Error} = \frac{(P_{est,max} - P_{est,onset}) - (P_{obs,max} - P_{obs,onset})}{P_{obs,max} - P_{obs,onset}} \times 100(\%) \qquad (5.3)$$

where P_{est} is the estimated pressure from the ultrasonic methods, and P_{obs} is the reference pressure measurement. P_{est} is averaged over sixteen cardiac cycles while P_{obs} is averaged over six cardiac cycles.

Although the flow-area plot in Figure 5-12 is plotted using the averaged flow velocity and diameter waveform assuming periodicity, it is more desirable to average

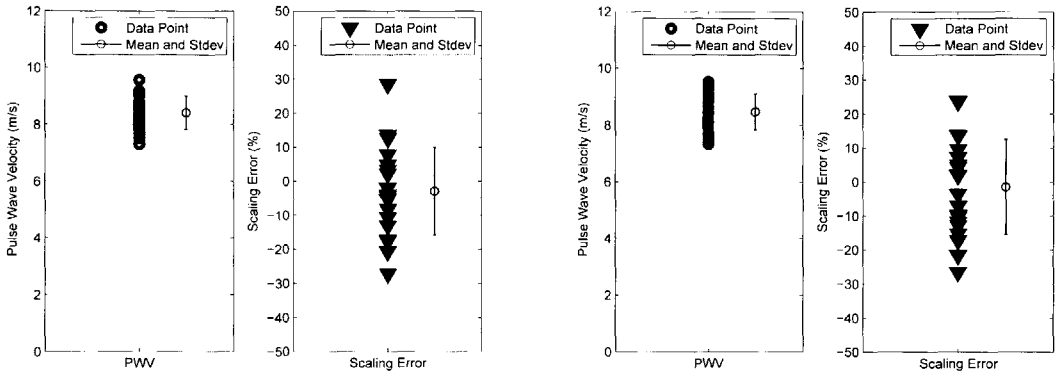

(a) Waveform averaging

(b) PWV averaging

Figure 5-14: Pulse wave velocity estimation statistics

the PWV estimates from each cardiac cycle because the heart rate may vary slightly between cycles in a physiological situation. Figure 5-14 shows the statistics of the estimated local PWV using the QA method. The PWVs are estimated from the averaged flow-area plot over sixteen cardiac cycles in Figure 5-14(a) while the other PWVs are estimated by averaging sixteen individual PWV estimate from a single cardiac cycle in Figure 5-14(b). Each point comes from data with sixteen cardiac cycles, and twenty independent data sets (from repetition of the same experiment) are plotted in the figure. Equivalently, the mean of the local PWV estimate in Figure 5-14(b) is an averaged PWV estimate over 320 cardiac cycles. The local PWV with the averaged flow-area plot results in 8.41±0.58 m/s while that of the PWV averaging is 8.47±0.63 m/s. Corresponding scaling errors are $-2.93 \pm 12.9\%$ and $-1.56 \pm 14.0\%$, respectively. An average scaling error is close to 0%, implying the true PWV to represent the elastic property of the latex rubber tube is about 8.47 m/s. In addition, the QA method accurately estimates the local PWV without a significant bias error. The variation of the local PWV estimate is mainly attributed to the variation of the spatial mean velocity estimate because of its stochastic nature, and it can be further suppressed with averaging over the greater number of cardiac cycles.

Flow-area plots are also obtained in different pulsatile pressure waveforms which emulate various heart rate conditions. Figure 5-15 shows the typical flow-area plots

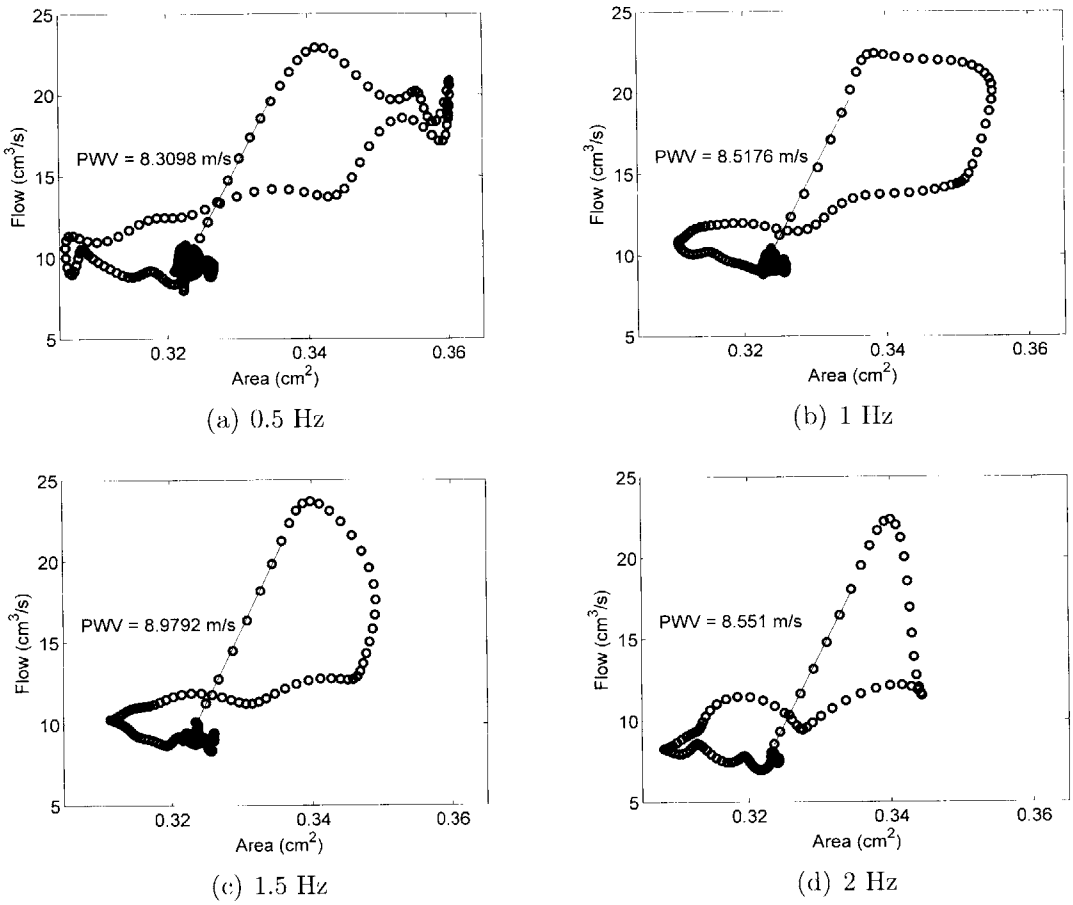

(a) 0.5 Hz (b) 1 Hz

(c) 1.5 Hz (d) 2 Hz

Figure 5-15: Measured flow-area plots in various pulsatile frequencies

from different pulsatile frequencies while maintaining the 10% duty cycle of the systolic phase. As the frequency increases, the shape of the flow-area plot after a linear phase changes because the pressure and the flow decrease caused by the end of the systolic phase is superimposed with the effect of the reflection at different timings. Nevertheless, the linear phase of each flow-area plot remains intact regardless of the pulsatile frequency. Therefore, the local PWV can be reliably estimated from the slope of the linear phase even in a varying heart rate condition as long as the early systolic phase is kept near reflection-free.

In addition, the length of the linear phase in the flow-area plot is compared between different observation sites along the latex rubber tube. Figure 5-16 shows the flow-area plots obtained from the different observation sites. The linear phase is

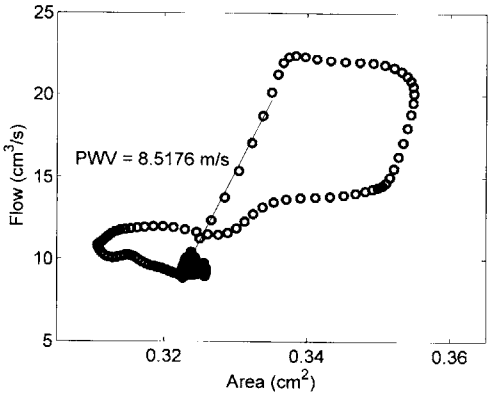

(a) Proximal site

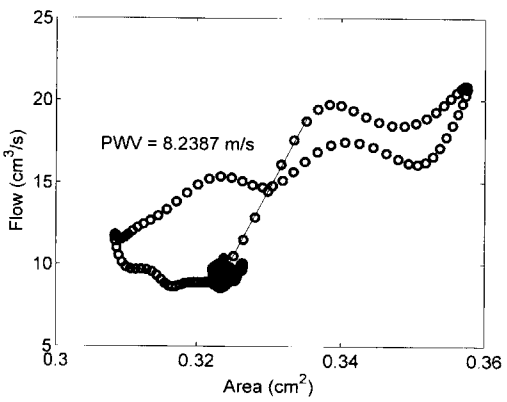

(b) Downstream from proximal site

Figure 5-16: Measured flow-area plot in different observation sites along a latex rubber tube

clearly shortened because a round trip time between the observation site and the reflection site is reduced. This result implies that a measurement site in an arterial tree is required to be sufficiently distant from a strong reflection site such as the arteriole to have a clear linear phase in a flow-area plot.

5.3.4 Pressure Waveform Comparison

This section presents the result of the complete pressure waveform estimation using ultrasonic methods. Equation 4.1 is slightly modified and re-written for the readability as:

$$P(t) - P_0 = \rho PWV^2 \ln(\frac{A(t)}{A_0}) \tag{5.4}$$

where ρ is the density of the BMF, A_0 and P_0 are a reference cross-sectional area and a pressure, respectively. A_0 and P_0 are measured 0.31 cm^2 and 39 mmHg, respectively in a constant flow setup.

Figure 5-17 shows comparisons between two pressure waveforms in various pressure conditions. The pressure waveform reconstructed from ultrasonic methods shows a good agreement with the reference waveform, and it tracks even the small change of pressure. This result shows that the diameter waveform which directly affects the shape of the estimated pressure waveform traces the small pressure change reliably.

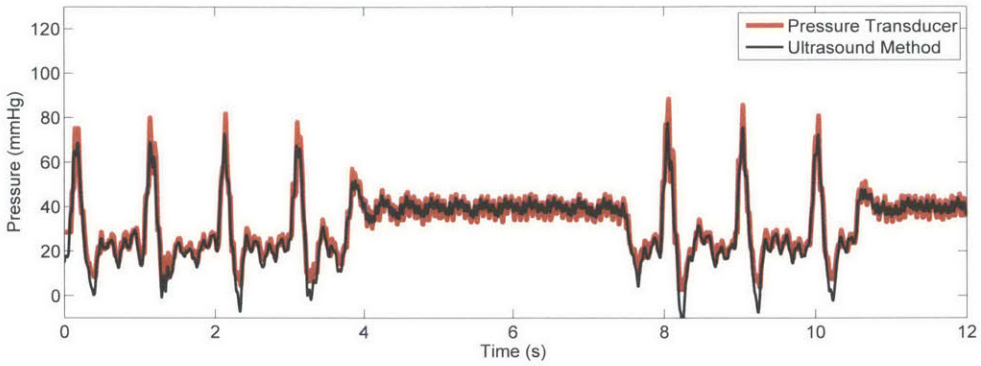

(a) Repeating pulsatile-constant pressure

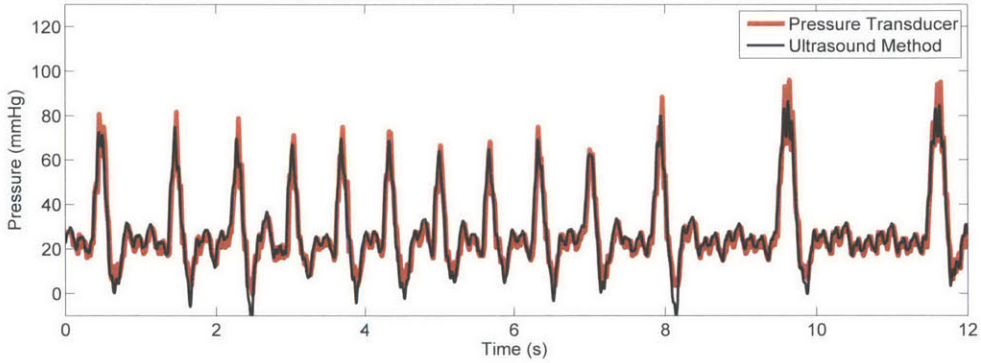

(b) Heart rate variation

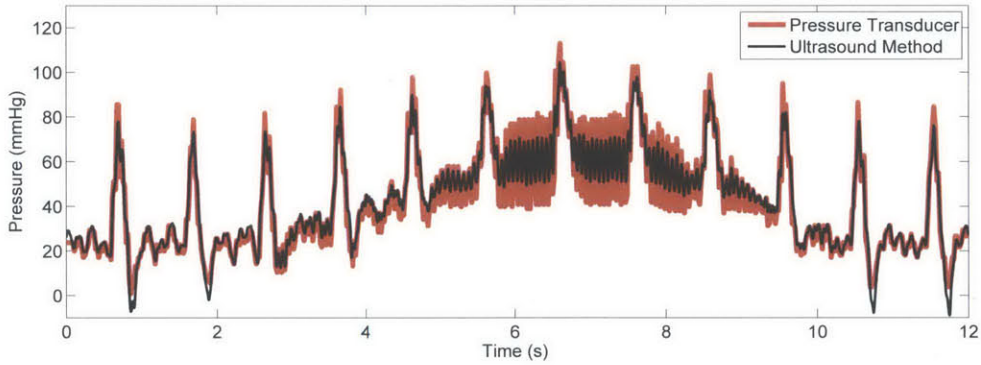

(c) Pressure baseline shift

Figure 5-17: Measured pressure waveform comparison in different pressure waveform setups

Combined with the accurate local PWV estimate, an entire pressure waveform is reliably reconstructed.

However, since the absolute diameter and the change of diameter waveform are not measured simultaneously, there exists ambiguity about which local minimum

point in the change of diameter waveform corresponds to the measured absolute minimum diameter. In this experiment, the absolute minimum diameter is separately measured in a 1 Hz pulsatile pressure setup. The same pulsatile pressure condition is intentionally included in all three cases of Figure 5-17 to use the separately measured minimum diameter as a reference. However, variation between each cardiac cycle causes the ambiguity in determining a correct baseline diameter. It is noteworthy that in Figure 5-17, a certain local minimum point is chosen which makes the best agreement between two waveforms. Therefore, two waveforms may have an offset error within the variation of minimum diameter measurements. However, this limitation is easily overcome with simultaneous measurements assisted by a higher data rate ultrasound system.

In the mean time, there is a notable discrepancy when the baseline pressure is high. This discrepancy is mainly attributed to the slow response of the latex rubber tube to internal pressure change when the pressure is varying fast. As mentioned in Section 5.1.1, the flow phantom generates high pressure by running its diaphragm motion quicker. Because of this limitation, the spectrum of the pressure waveform with an average high pressure has a strong high frequency component, and the diameter change does not respond fast enough to truthfully represent an internal pressure change. As a result, the amplitude of the diameter waveform, reflected in the pressure waveform from ultrasonic methods, is reduced while it still correctly tracks slowly a varying baseline pressure change. Fortunately, a normal ABP waveform is not expected to have such a high frequency component. Thus, this phenomenon is merely the artifact of the flow phantom. However, the effect of the viscoelasticity of arteries is worth of further investigation.

Chapter 6

Conclusion

6.1 Summary

In summary, this work introduces various ultrasonic methods to obtain a volumetric blood flow and vessel diameter waveform, and discusses the strengths and weaknesses of these methods. In addition, it validates the pressure estimation technique based on the two physiological waveforms acquired using ultrasonic methods in a custom-designed experimental setup.

The arterial system is physically modeled by a flow phantom that consists of a soft latex rubber tube and a pump, emulating an arterial vessel segment and the heart, respectively. The tube with a length of 30 cm and a diameter of 6.26 mm realistically models an artery (especially the common carotid artery) advancing toward the peripheral arterioles. In addition, the propagation of the pressure wave along the latex rubber tube mimics the pulse pressure wave propagation along an arterial tree. The reflection of the pressure wave, which occurs strongly at the arterioles, is achieved at the distal site of the rubber tube segment where the latex rubber tube meets a rigid connector, introducing sudden change in the elasticity and the cross-sectional area.

In this work, the volumetric flow rate of the blood mimicking fluid and the cross-sectional area of the tube are estimated simultaneously by using two single element transducers. Simultaneous measurement of these two parameters helps avoid the issue of synchronizing the two waveforms unless they are obtained simultaneously,

thereby making the QA method and the pressure estimation technique insensitive to beat-to-beat variation. In addition, this work demonstrates that the flow rate and the area waveform are obtained by using only two single element transducers. This demonstration relieves the need for high data rate and significant computational power that a typical array based ultrasound system requires, and shows potential for a non-invasive ABP waveform measurement device which has much smaller form factor than a commercially available ultrasound system.

This work clearly shows the existence of a reflection free period at the beginning of a cardiac cycle. As the QA method states, the pulse wave velocity of the latex rubber tube is estimated from the slope of a highly linear phase (implying near reflection free) in a flow-area plot. Its estimation accuracy is validated in direct comparison between two pressure waveforms (one from ultrasonic methods and the other from direct pressure measurement). The measurement results show that the pulse wave velocity truly quantifies the elastic property of the latex rubber tube and correctly establishes the mapping relation between the pulsatile change of cross-sectional area to the pressure waveform. Followed by the initial calibration of pressure and area measurements, the complete pressure waveform is accurately estimated.

6.2 Future Work

In the continuing research of this project, the following issues are expected to be addressed:

- **Transducer configuration design suitable for human subject testing**
  The geometry of two transducers relative to the latex rubber tube in the experiment is not realistic for the ABP waveform estimation in superficial arteries. In order to obtain sufficient uniformity in an acoustic beam pattern, a reduced aperture size is required. In addition, insonation angles of both transducers which affect not only the spatial mean velocity but the diameter measurement are difficult to obtain *in vivo*. Therefore, an algorithm to reliably identify insonation angles is required, and transducers should be positioned to accom-

modate its requirement. Finally, a proper transducer housing with acoustic coupling to the skin should be devised.

- **Clinical test**

  Although this work experimentally validates the ABP waveform estimation technique, a clinical test to prove the feasibility of the technique on human subjects is absolutely necessary. Potentially, the common carotid artery or the brachial artery can be selected as a measurement site. The clinical test provides the opportunity to verify ultrasonic measurements, the QA method and the overall ABP waveform estimation *in vivo*, while studying various effects due to the complicated vasculatures, the wave reflection and the non-ideality of arterial vessel walls.

- **Initial calibration for reference pressure**

  The necessity for initial calibration to get a reference pressure and a cross-sectional area challenges fully autonomous ABP waveform estimation desirable for CNAP (Continuous and Non-invasive Arterial Blood Pressure) monitoring device. An elastography based absolute blood pressure measurement technique or other techniques can be considered and discussed further.

- **Prototype design suitable for portable application**

  Prototype hardware implementation using discrete components is essential for the proof of concept of a portable CNAP monitoring device using ultrasound. The system level requirement to obtain necessary data in the clinical test should be specified. Potentially, the real-time operation of the introduced ABP waveform estimation as well as other display functionality may be validated using the prototype device. Finally, system level optimization may be incorporated to prove reasonable form factor and power consumption.

- **Integration of electronics**

  An integrated circuit (IC) technology eventually diminishes the dimension, power consumption and complexity of an ultrasound system. After its clin-

ical feasibility and system specification are fully defined with the prototype, both architecture level and block level circuit techniques may be incorporated into an application specific integrated circuit (ASIC) design for power efficient operation and performance improvement which truly enable a portable blood pressure estimation device.

Bibliography

[1] S. Mendis, P. Puska, B. Norrving, *et al.*, *Global atlas on cardiovascular disease prevention and control.* World Health Organization, 2011.

[2] S. S. Franklin, S. A. Khan, N. D. Wong, M. G. Larson, and D. Levy, "Is pulse pressure useful in predicting risk for coronary heart disease? The Framingham Heart Study," *Circulation*, vol. 100, pp. 354–360, July 1999.

[3] Y. Nakayama, K. Tsumura, N. Yamashita, K. Yoshimaru, and T. Hayashi, "Pulsatility of ascending aortic pressure waveform is a powerful predictor of restenosis after percutaneous transluminal coronary angioplasty," *Circulation*, vol. 101, pp. 470–472, Feb. 2000.

[4] R. Mukkamala, A. Reisner, H. Hojman, R. Mark, and R. Cohen, "Continuous cardiac output monitoring by peripheral blood pressure waveform analysis," *IEEE Transactions on Biomedical Engineering*, vol. 53, pp. 459–467, Mar. 2006.

[5] B. Haslam, T. Heldt, A. J. Gordhandas, C. Ricciardi, and G. Verghese, "Relating noninvasive cardiac output and total peripheral resistance estimates to physical activity in an ambulatory setting.," in *AAAI Spring Symposium: Computational Physiology*, 2011.

[6] G. Zhang, K. Ryan, C. Rickards, V. Convertino, and R. Mukkamala, "Early detection of hemorrhage via central pulse pressure derived from a non-invasive peripheral arterial blood pressure waveform," in *2012 Annual International Conference of the IEEE Engineering in Medicine and Biology Society (EMBC)*, pp. 3116–3119, Aug. 2012.

[7] G. M. Drzewiecki, J. Melbin, and A. Noordergraaf, "Arterial tonometry: Review and analysis," *Journal of Biomechanics*, vol. 16, no. 2, pp. 141–152, 1983.

[8] L. M. Van Bortel, E. J. Balkestein, J. J. van der Heijden-Spek, F. H. Vanmolkot, J. A. Staessen, J. A. Kragten, J. W. Vredeveld, M. E. Safar, H. A. S. Boudier, and A. P. Hoeks, "Non-invasive assessment of local arterial pulse pressure: comparison of applanation tonometry and echo-tracking," *Journal of Hypertension June 2001*, vol. 19, no. 6, pp. 1037–1044, 2001.

[9] J. Penaz *et al.*, "Photoelectric measurement of blood pressure, volume and flow in the finger," in *Digest of the 10th international conference on medical and biological engineering*, vol. 104, 1973.

[10] B. P. M. Imholz, G. a. V. Montfrans, J. J. Settels, G. M. a. V. D. Hoeven, J. M. Karemaker, and W. Wieling, "Continuous non-invasive blood pressure monitoring: reliability of finapres device during the valsalva manoeuvre," *Cardiovascular Research*, vol. 22, pp. 390–397, June 1988.

[11] B. Silke and D. McAuley, "Accuracy and precision of blood pressure determination with the finapres: an overview using re-sampling statistics," *Journal of Human Hypertension*, vol. 12, p. 403, June 1998.

[12] J. Jensen and N. Svendsen, "Calculation of pressure fields from arbitrarily shaped, apodized, and excited ultrasound transducers," *IEEE Transactions on Ultrasonics, Ferroelectrics and Frequency Control*, vol. 39, pp. 262–267, Mar. 1992.

[13] J. A. Jensen, "Field: A program for simulating ultrasound systems," in *10th Nordicbaltic Conference on Biomedical Imaging*, vol. 34, pp. 351–353, 1996.

[14] T. L. Szabo, *Diagnostic ultrasound imaging : inside out / Thomas L. Szabo.* Academic Press series in biomedical engineering, Burlington, MA : Elsevier Academic Press, 2004.

[15] J. A. Jensen, *Estimation of blood velocities using ultrasound : a signal processing approach / Jrgen Arendt Jensen.* Cambridge ; New York, USA : Cambridge University Press, 1996.

[16] W. N. McDicken, *Diagnostic ultrasonics : principles and use of instruments / W. N. McDicken.* Wiley medical publication, New York : Wiley, 1981.

[17] F. W. Kremkau, *Diagnostic ultrasound: principles and instruments.* Philadelphia, Pa.: W.B. Saunders, 1998.

[18] F. A. Duck, A. C. Baker, and H. C. Starritt, *Ultrasound in medicine / edited by Francis A. Duck, Andrew C. Baker, Hazel C. Starritt.* Medical science series, Bristol ; Philadelphia, Pa. : Institute of Physics Pub., 1998.

[19] K. K. Shung, R. Sigelmann, and J. Reid, "Scattering of ultrasound by blood," *IEEE Transactions on Biomedical Engineering*, vol. BME-23, pp. 460–467, Nov. 1976.

[20] G. S. Kino, *Acoustic waves : devices, imaging, and analog signal processing / Gordon S. Kino.* Prentice-Hall signal processing series, Englewood Cliffs, N.J. : Prentice-Hall, 1987.

[21] W. P. Mason, *Electromechanical transducers and wave filters.* Bell Telephone Laboratories series, New York, D. Van Nostrand Co., 1948.

[22] R. Krimholtz, D. Leedom, and G. Matthaei, "New equivalent circuits for elementary piezoelectric transducers," *Electronics Letters*, vol. 6, pp. 398–399, June 1970.

[23] B. A. Auld, *Acoustic fields and waves in solids / B.A. Auld.* Malabar, Fla. : R.E. Krieger, 1990.

[24] W. R. Milnor, *Hemodynamics / William R. Milnor.* Baltimore : Williams & Wilkins, 1989.

[25] J. R. Womersley, "Method for the calculation of velocity, rate of flow and viscous drag in arteries when the pressure gradient is known," *The Journal of Physiology*, vol. 127, pp. 553–563, Mar. 1955.

[26] J. Womersley, "XXIV. oscillatory motion of a viscous liquid in a thin-walled elastic tubeI: the linear approximation for long waves," *Philosophical Magazine Series 7*, vol. 46, no. 373, pp. 199–221, 1955.

[27] J. K.-J. Li, *Arterial system dynamics / John K-J. Li.* New York University biomedical engineering series, New York : New York University Press, 1987.

[28] E. N. Marieb, P. B. Wilhelm, and J. Mallatt, *Human anatomy / Elaine N. Marieb, Patricia Brady Wilhelm, Jon Mallatt.* Boston [Mass.] : Pearson, 2014.

[29] C. D. Clemente, *Anatomy : a regional atlas of the human body / Carmine D. Clemente.* Baltimore : Williams & Wilkins, 1997.

[30] J. Krejza, M. Arkuszewski, S. E. Kasner, J. Weigele, A. Ustymowicz, R. W. Hurst, B. L. Cucchiara, and S. R. Messe, "Carotid artery diameter in men and women and the relation to body and neck size," *Stroke*, vol. 37, pp. 1103–1105, Apr. 2006.

[31] J. A. Levenson, P. A. Peronneau, A. Simon, and M. E. Safar, "Pulsed doppler: determination of diameter, blood flow velocity, and volumic flow of brachial artery in man," *Cardiovascular Research*, vol. 15, pp. 164 170, Mar. 1981.

[32] S. Meaume, A. Benetos, O. F. Henry, A. Rudnichi, and M. E. Safar, "Aortic pulse wave velocity predicts cardiovascular mortality in subjects >70 years of age," *Arteriosclerosis, Thrombosis, and Vascular Biology*, vol. 21, pp. 2046–2050, Dec. 2001.

[33] T. W. Hansen, J. A. Staessen, C. Torp-Pedersen, S. Rasmussen, L. Thijs, H. Ibsen, and J. Jeppesen, "Prognostic value of aortic pulse wave velocity as index of arterial stiffness in the general population," *Circulation*, vol. 113, pp. 664 670, Feb. 2006.

[34] J. Blacher, R. Asmar, S. Djane, G. M. London, and M. E. Safar, "Aortic pulse wave velocity as a marker of cardiovascular risk in hypertensive patients," *Hypertension*, vol. 33, pp. 1111–1117, May 1999.

[35] R. Hoctor, A. Dentinger, and K. Thomenius, "Array signal processing for local arterial pulse wave velocity measurement using ultrasound," *IEEE Transactions on Ultrasonics, Ferroelectrics and Frequency Control*, vol. 54, pp. 1018–1027, May 2007.

[36] J. Luo, R. Li, and E. Konofagou, "Pulse wave imaging of the human carotid artery: an in vivo feasibility study," *IEEE Transactions on Ultrasonics, Ferroelectrics and Frequency Control*, vol. 59, pp. 174–181, Jan. 2012.

[37] P. J. Brands, J. M. Willigers, L. A. F. Ledoux, R. S. Reneman, and A. P. G. Hoeks, "A noninvasive method to estimate pulse wave velocity in arteries locally by means of ultrasound," *Ultrasound in Medicine & Biology*, vol. 24, pp. 1325–1335, Dec. 1998.

[38] J. M. Meinders, L. Kornet, P. J. Brands, and A. P. G. Hoeks, "Assessment of local pulse wave velocity in arteries using 2D distension waveforms," *Ultrasonic Imaging*, vol. 23, pp. 199–215, Oct. 2001.

[39] S. I. Rabben, N. Stergiopulos, L. R. Hellevik, O. A. Smiseth, S. Slrdahl, S. Urheim, and B. Angelsen, "An ultrasound-based method for determining pulse wave velocity in superficial arteries," *Journal of Biomechanics*, vol. 37, pp. 1615–1622, Oct. 2004.

[40] R. Williams, A. Needles, E. Cherin, F. Foster, Y.-Q. Zhou, and M. Henkelman, "A retrospective method for pulse-wave velocity measurement in the mouse," in *2005 IEEE Ultrasonics Symposium*, vol. 1, pp. 381–384, Sept. 2005.

[41] B. W. A. M. M. Beulen, N. Bijnens, G. G. Koutsouridis, P. J. Brands, M. C. M. Rutten, and F. N. van de Vosse, "Toward noninvasive blood pressure assessment in arteries by using ultrasound," *Ultrasound in Medicine & Biology*, vol. 37, pp. 788–797, May 2011.

[42] S. Vullimoz, N. Stergiopulos, and R. Meuli, "Estimation of local aortic elastic properties with MRI," *Magnetic Resonance in Medicine*, vol. 47, no. 4, pp. 649–654, 2002.

[43] H.-H. Peng, H.-W. Chung, H.-Y. Yu, and W.-Y. I. Tseng, "Estimation of pulse wave velocity in main pulmonary artery with phase contrast MRI: preliminary investigation," *Journal of Magnetic Resonance Imaging*, vol. 24, no. 6, pp. 1303–1310, 2006.

[44] E.-S. H. Ibrahim, K. R. Johnson, A. B. Miller, J. M. Shaffer, and R. D. White, "Measuring aortic pulse wave velocity using high-field cardiovascular magnetic resonance: comparison of techniques," *Journal of cardiovascular magnetic resonance: official journal of the Society for Cardiovascular Magnetic Resonance*, vol. 12, no. 1, pp. 26–39, 2010.

[45] L. L. Huntsman, D. K. Stewart, S. R. Barnes, S. B. Franklin, J. S. Colocousis, and E. A. Hessel, "Noninvasive doppler determination of cardiac output in man. clinical validation.," *Circulation*, vol. 67, pp. 593–602, Mar. 1983.

[46] R. W. Gill, "Measurement of blood flow by ultrasound: Accuracy and sources of error," *Ultrasound in Medicine & Biology*, vol. 11, pp. 625–641, July 1985.

[47] C. F. Hottinger and J. D. Meindl, "Blood flow measurement using the attenuation-compensated volume flowmeter," *Ultrasonic Imaging*, vol. 1, pp. 1 15, Jan. 1979.

[48] R. W. Gill, "Pulsed doppler with b-mode imaging for quantitative blood flow measurement," *Ultrasound in Medicine & Biology*, vol. 5, no. 3, pp. 223–235, 1979.

[49] D. W. Holdsworth, C. J. D. Norley, R. Frayne, D. A. Steinman, and B. K. Rutt, "Characterization of common carotid artery blood-flow waveforms in normal human subjects," *Physiological Measurement*, vol. 20, p. 219, Aug. 1999.

[50] A. P. G. Hoeks, C. Willekes, P. Boutouyrie, P. J. Brands, J. M. Willigers, and R. S. Reneman, "Automated detection of local artery wall thickness based on m-line signal processing," *Ultrasound in Medicine & Biology*, vol. 23, no. 7, pp. 1017–1023, 1997.

[51] R. W. Stadler, J. Andrew Taylor, and R. S. Lees, "Comparison of b-mode, m-mode and echo-tracking methods for measurement of the arterial distension waveform," *Ultrasound in Medicine & Biology*, vol. 23, no. 6, pp. 879–887, 1997.

[52] A. P. G. Hoeks, P. J. Brands, F. A. M. Smeets, and R. S. Reneman, "Assessment of the distensibility of superficial arteries," *Ultrasound in Medicine & Biology*, vol. 16, no. 2, pp. 121–128, 1990.

[53] A. Hoeks, Xu Di, P. Brands, and R. Reneman, "An effective algorithm for measuring diastolic artery diameters," *Archives of Acoustics*, vol. 20, pp. 65–76, Jan. 1995.

[54] A. P. G. Hoeks, P. J. Brands, J. M. Willigers, and R. S. Reneman, "Non-invasive measurement of mechanical properties of arteries in health and disease," *Proceedings of the Institution of Mechanical Engineers, Part H: Journal of Engineering in Medicine*, vol. 213, pp. 195–202, Mar. 1999.

[55] P. G. M. de Jong, T. Arts, A. P. G. Hoeks, and R. S. Reneman, "Determination of tissue motion velocity by correlation interpolation of pulsed ultrasonic echo signals," *Ultrasonic Imaging*, vol. 12, pp. 84 98, Apr. 1990.

[56] A. P. G. Hoeks, T. G. J. Arts, P. J. Brands, and R. S. Reneman, "Comparison of the performance of the RF cross correlation and doppler autocorrelation technique to estimate the mean velocity of simulated ultrasound signals," *Ultrasound in Medicine & Biology*, vol. 19, no. 9, pp. 727 740, 1993.

[57] P. J. Brands, A. P. G. Hoeks, L. A. F. Ledoux, and R. S. Reneman, "A radio frequency domain complex cross-correlation model to estimate blood flow velocity and tissue motion by means of ultrasound," *Ultrasound in Medicine & Biology*, vol. 23, no. 6, pp. 911–920, 1997.

[58] K. V. Ramnarine, D. K. Nassiri, P. R. Hoskins, and J. Lubbers, "Validation of a new blood-mimicking fluid for use in doppler flow test objects," *Ultrasound in Medicine & Biology*, vol. 24, pp. 451–459, Mar. 1998.

[59] S. J. Pietrangelo, *An electronically steered, wearable transcranial doppler ultrasound system.* Thesis, Massachusetts Institute of Technology, 2013. Thesis (S.M.)–Massachusetts Institute of Technology, Dept. of Electrical Engineering and Computer Science, 2013.